Experimental Hydrodynamics of Spherical Projectiles Impacting On a Free Surface Using High Speed Imaging Techniques

By

Stephen Michael Laverty Jr.

B.S., Mechanical Engineering
Brigham Young University, 2003

SUBMITTED TO THE DEPARTMENT OF OCEAN ENGINEERING IN PARTIAL FULFILLMENT OF THE REQUIREMENTS FOR THE DEGREE OF

MASTER OF SCIENCE IN OCEAN ENGINEERING
AT THE
MASSACHUSETTS INSTITUTE OF TECHNOLOGY

SEPTEMBER 2004

Author ……...…….
Stephen M. Laverty Jr.
Department of Ocean Engineering
Massachusetts Institute of Technology
August 8, 2004

Certified by ……...……
Alexandra H. Techet
Assistant Professor of Ocean Engineering
Massachusetts Institute of Technology
Thesis Supervisor

Accepted by ……...……...
Michael S. Triantafyllou
Chairman, Departmental Committee on Graduate Studies
Massachusetts Institute of Technology
Department of Ocean Engineering

Experimental Hydrodynamics of Spherical Projectiles Impacting On a Free Surface Using High Speed Imaging Techniques

By

Stephen Michael Laverty Jr.

Submitted to the Department of Ocean Engineering
On August 8, 2004 in Partial Fulfillment of the
Requirements for the Degree of Master of Science in
Ocean Engineering

ABSTRACT

This thesis looks at the hydrodynamics of spherical projectiles impacting the free surface using a unique experimental WebLab facility. Experiments were performed to determine the force impact coefficients of spheres and then compare obtained results to theories developed by Von-Karman [19] and Wagner [20]. It was found that experimental results matched a generalized Wagner approach developed by Touvia Miloh [12].

A critical impact speed for splash formation was determined before which no splash cavity would form. The cone angle formed behind an impacting object was also studied. The cone angle was found to be a function of depth and impact speed over the range of impact velocities tested. Steel spheres ranging in diameter from 0.64 cm (¼ in) to 5.08 cm (2 in) were used at impact speeds from 0 to 6.9 m/s. Standard billiard balls of diameter 5.72cm (2.25 in) were also used in this study.

As part of this project, the WebLab facility was constructed. iMarine WebLab is an interactive teaching tool used to educate students in various aspects of marine hydrodynamics and experimental fluid mechanics.

Thesis Supervisor: Alexandra H. Techet
Assistant Professor of Ocean Engineering
Massachusetts Institute of Technology

Acknowledgements

I would in no way be able to accomplish this goal without the love and support of my family, friends and colleagues. I would especially like to express appreciation to my loving wife for all of her support and patience through the long days and endless nights of homework and studying. I would like to thank my thesis advisor, Alex Techet for her guidance and direction throughout my academic career and during this project. I would also like to thank those who helped me perform the experiments and interpret the data presented herein, namely Dr. Richard Kimball, Alex Techet, Cynthia Chi, Julie Finkelstein and Jacob Temme. Thanks also go out to my lab partner and good friend, Tadd Truscott for his help and support through this project. This thesis represents the completion of my greatest academic goal. For this I will be eternally grateful.

Table of Contents

List of Figures

Chapter 1

Introduction

1.0 – Motivation

The impact of objects on a free surface is quite complex. This problem has piqued the interest of researchers for centuries and remains of interest today. Water impact phenomena are prevalent in ship slamming, various military applications, and biological problems such as lizards walking on the free surface. The physics surrounding the moment of impact are investigated in this thesis using spherical objects. Data obtained can then be used as a springboard for further experiments related to ship slamming and other applications.

Naval architects require a knowledge of the hydrodynamics and impact loads a ship will encounter in a seaway during the initial design stages of any ocean vessel. These hydrodynamic impact loads have resulted in failure of ocean going vessels [1, 4, 8, 10, 18]. To get preliminary estimates of these forces, impact tests can be performed and the results can be applied to improve the ship's design. The impact force coefficients for spheres over a range of impact velocities are discussed herein and compared to theories developed by Von-Karman [19] and Wagner [20]. The splash angle formed at the initial

stages of impact as a function of impact speed is also investigated. To facilitate the study of this complex problem, we developed an interactive teaching tool allowing remote users from around the world to conduct experiments from the safety of their own lab or classroom.

1.1 – Surface Impact

Surface impact of objects results in a complex series of hydrodynamic events. This series of events is consistent over a range of object sizes and entry speeds once a critical splash inception velocity is reached. The sequence includes the moment of impact, splash inception, cavity formation, surface seal, and bubble pinch off. A typical sequence of events for a billiard ball of diameter 5.72 cm (2.25 in) impacting the free surface is shown in figure 1.1. Here, the initial velocity of the ball at impact is 4 m/s and a high speed video camera captured the events at 628 frames per second (fps). Figure 1.1 displays every 10^{th} frame separated by 0.016 seconds in time.

At the moment of impact (figure 1.1a), a sudden change in the pressure gradient is formed at the water surface and water under and near the object is accelerated downward. A cavity is formed behind the object as it descends through the water (figure 1.1b), and the splash at the surface has a changing velocity component which starts radialy outward. The splash begins to move upward (figure 1.1c) and then radialy inward (figure 1.1d) before it finally domes over and seals the cavity at the surface (figure 1.1e). This is known as surface seal. Surface seal is one of the most important occurrences in cavity development and has great influence on later cavity growth [9]. The closed cavity continues to grow in length until the hydrostatic and dynamic pressures of the surrounding fluid cause the cavity to pinch off at an intermediate depth. The inception of the pinch off is seen in figure 1.1g and figure 1.1h shows a completely separate cavity.

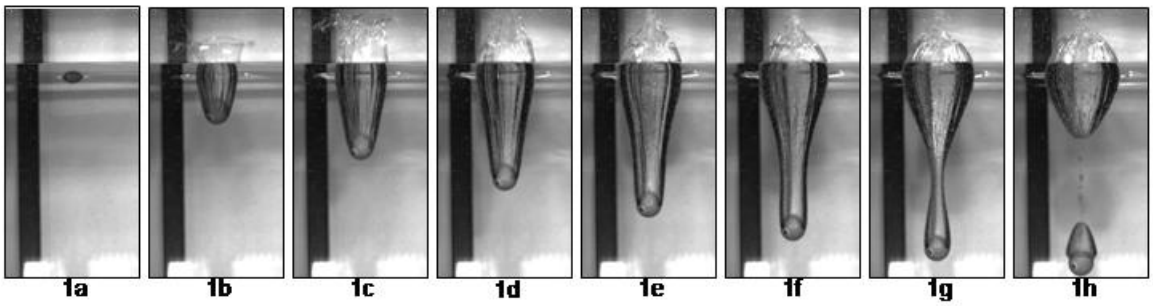

Figure 1.1 – High speed camera images of a 5.72 cm (2.25 in) billiard ball entering water at 4 m/s. The camera frame rate was 629 frames per second. Every tenth frame is included here, which gives an effective rate of 63 frames per second.

The three dimensional water surface impact problem is a very complex one. This thesis studies the first moments of impact where the sphere has entered up to half of its diameter. It is in this short amount of time that the most interesting phenomena transpire. In practice, simplifying assumptions are applied to the three dimensional problem reducing it to a two dimensional problem, that can be solved using strip theory. This simplifies the governing equations but introduces error. In general, strip theory assumes sufficient cross sectional uniformity along the length of the body to allow for segmentation, such as in long tubes or cylinders. Each segment is also assumed to act independently from the other segments such that the fluid behavior around one strip does not affect the neighboring strip. The segmented two dimensional solutions are then integrated along the length of the body to yield the full solution.

Strip theory can not be applied to spheres due to the non-uniformity of the cross section and because the assumption of a two dimensional flow field around the sphere is not valid. Spheres represent an extreme case, where three dimensional effects are significant. This is one reason why most solutions to sphere impact problems have been found using experimental techniques. Examples of using two dimensional techniques to simplify three dimensional problems can be found from Ochi [16] and Newman [15].

1.2 – Previous Studies of Surface Impact

Ground breaking work in splash formation was first performed by Worthington [23] in 1903. In his study, Worthington used single spark photography to capture images of the splash cavity created by falling objects. High speed motion-picture studies were later performed by Gilbarg and Anderson [5] at the Naval Ordnance Laboratory in 1948. In their experiment, steel spheres ranging is size from ¼-in. to 1-in. were shot at high speeds into a pressure controlled tank. Their study focused on the dependence of air-water entry cavities on the atmospheric pressure over the water surface. It was concluded that surface closure is the most important event in the development of the water cavity and greatly influences later cavity growth. It was also found that Froude scaling held true in the region of low Froude numbers (1-80) and low atmospheric pressures where the Froude Number is defined as:

$$F_r = \frac{V_I}{\sqrt{gd}}, \qquad [1.1]$$

where V_I is the impact velocity, g is the gravitational constant, and d is the sphere diameter. The basic experimental setup used in our present study is similar to the one used by Gilbarg and Anderson[5].

Further investigations were performed by Albert May [9] in 1952 using a similar experimental setup. May examined the effect of density and atmospheric pressure above the water, and the velocity, size, and nose shape of the projectile on the time and location of surface closure. It was found that Froude scaling was a good first approximation in describing cavity behavior. Some improvement can be made on this approximation with pressure and density scaling of the surrounding air. It was also concluded that the cavity shape was not dependent on the nose shape of the projectile for a given drag force.

A biological air-water impact study was performed by Glasheen and McMahon [6] in 1996. This study focused on the ability of the Basilisk lizard to “walk” on water. High speed video and force gauges were used to determine the forces produced during the

impact and open-cavity phases of low speed water entry. Disks, representing the lizard's feet, were shot into water and reactions were studied. It was found that the period between impact and cavity closure could be modeled by a single value of dimensionless time. It was also concluded that the fundamental phenomena associated with low-speed water entry of a disk can be characterized by dimensionless drag, time, and mass parameters.

A mathematical approach to solving 3-dimensional water impact problems has been attempted by many scholars but solutions have modeled experimental results only under stringent assumptions. Wantabe [21, 22] derived a general expression for the impact forces on a falling cylinder. This model included assumptions such as negligible gravity at the free surface, negligible flow variation in the vertical direction along the body, and an undisturbed water surface. These are the same assumptions made by Von-Karman [19]. Another issue which arises in 3-dimensional analysis of water impact problems is the thin layer of air that is trapped between the object and the free surface during impact. This air cushion acts as a damper which changes the dynamics of the impact problem. This becomes very important as the striking surface becomes blunter. This occurs on flat bottomed objects such as many hull forms and flat plates. At the time of this thesis, a general solution to this phenomenon has not yet been derived.

High speed photography and experimentation have been and still remain the foremost methods of determining characteristics of water impact. Dr. Harold Edgerton [17] was one of the first scientists to use artificial lighting to take high speed pictures of fast moving objects. Edgerton first became famous for using stroboscopic photography to take high speed pictures of rotating turbo machinery. The synchronized strobe lights used were capable of flashing at rates of over 100,000 frames per second. That is faster than even the best mechanical shutters available today. A dark room was used and the camera shutter remained open during the entire event of interest. Film passed by the open shutter at high speeds making the strobe lights themselves act as the shutter. Photography is now entering the digital world, which allows for faster developing of images without the use of film. Advances in high speed digital photography have

enabled an increased understanding of water impact with the aid of higher frame rates and increased optical clarity.

1.3 – WebLab

Research presented herein was performed using the MIT iMarine WebLab setup. The purpose of the water surface impact WebLab is to teach marine hydrodynamic concepts through laboratory experiences. Weblab allows users to remotely run experiments similar to the ones performed in this thesis and to process acquired data off-line with additional supporting data from computational simulations available on-line. The learning objectives include conceptualizing the physics of free surface impact and then interpreting the output data to arrive at desired conclusions.

The design of the impact WebLab allows for the study of a variety of object shapes such as spheres, cylinders, wedges, or blocks. Remote users dictate inputs which add flexibility to the experimental design. Such input parameters include impact velocity, angle of impact, video capture rates and choice of instrumentation. All data except for images are saved in text format for later processing. This allows for integration with third party numerical codes and comparison with theoretical materials. Thus, WebLab is a comprehensive and versatile teaching tool.

The WebLab impact laboratory setup consists of an automated loading mechanism that releases objects between two rotating wheels, which then shoots the objects into a tank of water at speeds of up to 20 m/s. The loading and shooting mechanisms are connected to an aluminum frame which is supported above the tank by a steel support structure. The platform has two degrees of freedom, rotational and linear, allowing different angles of impact. Components of the WebLab facility were also designed as part of this thesis.

1.4 – Chapter Preview

Design processes and experimental data are presented in the following chapters. Chapter two discusses the experimental setup used to conduct these experiments as well as the

design of specific WebLab components. Chapter 3 examines impact force coefficients over a range of impact velocities. Several theoretical models are presented and compared to the acquired data. Chapter 4 explores the formation of the splash cavity for different size spheres at different impact velocities. Chapter 5 contains a summary of conclusions made during this thesis, interesting phenomena encountered during experimentation, and possible subjects of future research.

Chapter 2

Experimental Methods

2.0 – Introduction

The MIT i-Marine WebLab facility was designed primarily as a teaching tool. Using an integrated control system, the experiments can be run remotely through a web interface. The goal was to allow students across the globe to have access to modern experimental hydrodynamic facilities and to increase naval architecture educational resources in the United States. This WebLab facility was used to investigate the impact of objects on the free surface.

The impact laboratory setup consists of an automated loading mechanism that releases objects between two rotating wheels, which shoots the objects into a 0.9m wide x 1.5m long x 1.8m deep tank of water at speeds of up to 20 m/s. The loading and shooting mechanisms are connected to an aluminum frame which is supported above the tank by a steel support structure. The platform has two degrees of freedom, rotational and linear, which are controlled by two stepper motors. This allows for constant impact location for variable angles of attack. Figure 2.1 shows the main components of the experimental setup. The loading mechanism, sensory equipment, motion control and LabView programming of these devices will be discussed in the following sections.

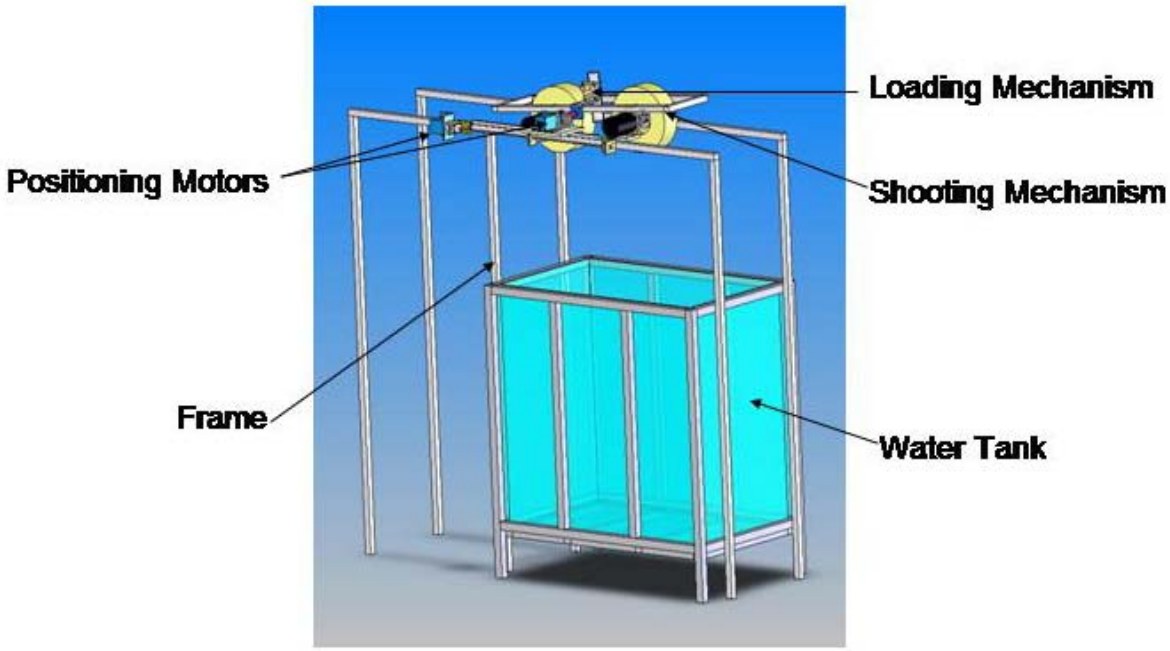

Figure 2.1 – Conceptual drawing of the experimental setup with tank, support structure, loader, and shooter. Stepper motors controlled the horizontal and angular position of the shooting platform which allowed for variable angles of impact.

2.1 – Loading Mechanism

To allow remote operation of WebLab, an automatic loader was designed specifically for the chosen projectiles. The spherical objects chosen for the WebLab impact experiment were standard billiard balls, which have a diameter of 5.72 cm (2.25 in), weigh 17 g each and are made of a phenolic resin. The loading mechanism holds, and then releases, the projectiles upon computer command. Parameters considered during the pre-design phase were timing, number of balls the mechanism was to hold, mounting of the loader, ease of reloading, compatibility with the LabView control system and cost efficiency.

The loader was designed to drop the balls directly above and centered over the spinning wheels of the shooting mechanism. Several design concepts were considered to accomplish this task. The first design was a carousel type loader which contained several columns of balls in a solid cylinder which would then rotate over a hole to release a single ball (Figure 2.2a). Another concept involved using a track made of standard V-channel which held the balls. The balls could then be released with a mechanical trigger

(Figure 2.2b). The third concept involved a vertical PVC pipe to hold the balls with a mechanical release mechanism to allow one ball to fall at a time (Figure 2.2c). Examples of these preliminary loading designs are shown below in Figure 2.2.

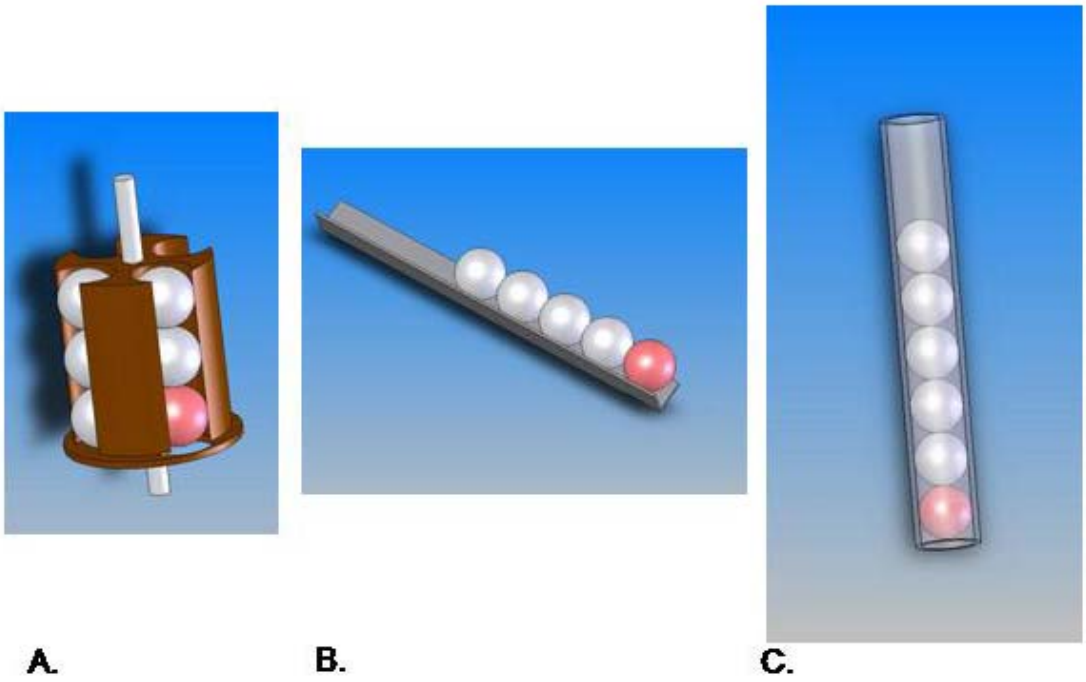

Figure 2.2 – Three preliminary concepts for release mechanisms which include:

A. Rotating carousel loader

B. Inclined V-channel loader

C. Vertical pipe loader

Upon evaluation of the three concepts, it was decided to proceed with the vertical pipe concept. The carousel type loader would be accurate and had the potential of easy loading but would require an additional stepper motor, expensive material, and complex machining. While this design met most specifications, it did not fit within the budget. The V-channel design was simple and inexpensive but would not be capable of the required accuracy. The balls had the potential of rolling into, not dropping directly over, the spinning wheels. This would cause a component of velocity away from the path of the spinning wheels. The vertical pipe design was simple and would also satisfy all of our requirements. The pipe could contain a full set of billiard balls (16) and drop them directly over the spinning wheels. A simple mechanical trigger could be attached to this

design as a release mechanism. For these reasons it was decided to proceed with the vertical pipe design.

Control of the release mechanism was achieved through LabView software to allow for ease of compatibility between the other system components. A National Instruments PCI-7342 motion control board contains both digital and analog outputs that can operate simple electrical components. Electric solenoids, which are digital in operation, were chosen to drive the mechanical release mechanism. The solenoid mount was designed so that no additional parts would be needed to hold the balls in place. Two generic pull style intermediate duty solenoids were purchased, which accomplished this design. The solenoids require a 24 volt power source and 2.5 amps of current.

The release mechanism firing cycle is shown in Figure 2.3. In the default position the upper piston supports all of the balls in the loader. When triggered, the upper piston retracts to allow the balls to drop onto the lower piston. The upper piston is then released and supports all of the balls except for the one ready to be dropped. Finally, the lower piston retracts to release the ball over the spinning wheels. The cycle is then repeated for the remaining balls.

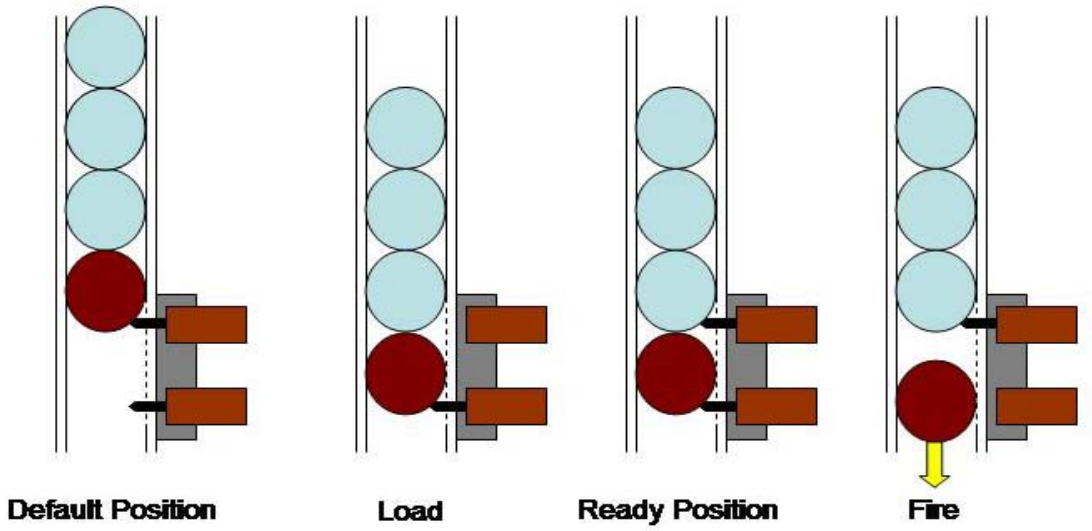

Figure 2.3 – Projectile release sequence showing 4 stages of firing and loading.

While the majority of the force from the weight of the pool balls is in the vertical direction, a horizontal force component exists on the solenoid pistons due to the curvature of the balls. Thus, the upper solenoid requires the greater return force to raise the remaining balls into the ready position (see Figure 2.3). A Solenoid with 140 oz of force was chosen for this application, which was sufficient to raise the remaining balls.

In order for the solenoids to return to the default position, a mechanical return was necessary. To accomplish this, springs were attached to the solenoid piston as seen in figure 2.4. Conical compression springs were chosen for this application. Two springs were used together on the upper solenoid to further increase the return force. A ¼ inch compression of the springs produced a return force of 68 oz.

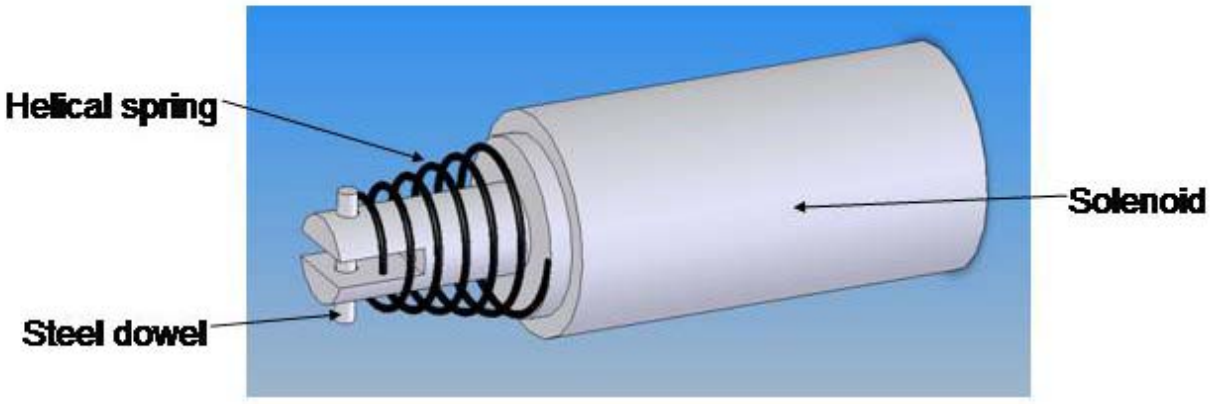

Figure 2.4 – Conceptual drawing of the mechanical spring return. Standard conical compression springs were attached to an electric pull-style solenoid.

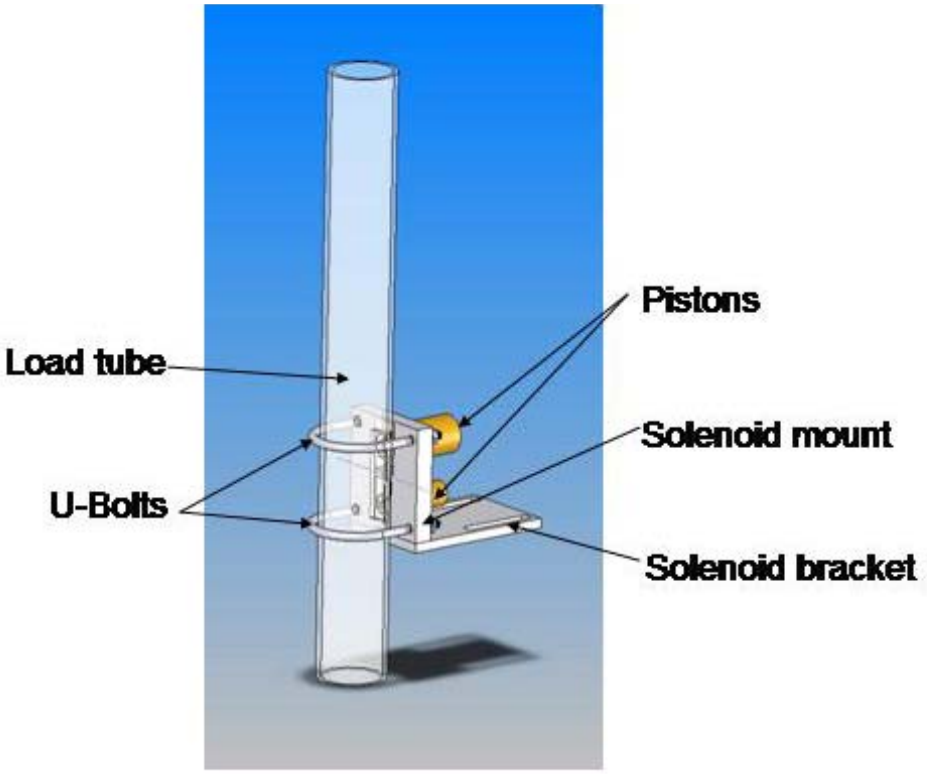

Figure 2.5 – Solid Works model of the loading mechanism which is able to hold up to 16 standard pool balls and can be adapted for the use of various sized projectiles.

Standard U-bolts were chosen to hold the load tube securely to the solenoid mount and the solenoid bracket was designed to attach the loader assembly to the shooter structure. Since this lab can be run via the World Wide Web and viewed through a live web cam, the load tube material was chosen to be transparent acrylic so the loading process can be observed by the remote user. The solenoid bracket was designed with mounting slots for both alignment purposes and to accommodate various projectile sizes for future experiments. The final loading mechanism is shown in Figure 2.5. The total cost of the mechanism was under $100.

The hardware used to actuate the loading mechanism included a National Instruments NI-DAQ PCI-MIO-16E-4 data acquisition card with 8 digital, 5 Volt output modules. An SSR 70RCK8 backplane and two 60-Volt DC relays were purchased through National Instruments, which allowed for control of the two solenoids. The 24 Volts required by the solenoids were connected to the relay and the control of the relay was governed by

the output 5 Volts from LabView through the backplane. A 5 Volt signal to the relay closed the circuit of the solenoid and retracted the piston. A 0 Volt signal opened the circuit and the piston returned to its default position.

LabView controlled the operation and timing of the solenoid's firing cycle. Control of the top and bottom solenoids was governed by the analog output channels 0 and 1 respectively. LabView code was written using a sequence structure. When triggered, channel 0 is switched on followed by a 750 millisecond wait. This allows the top solenoid to engage for that wait period. Channel 0 is then switched back to the default off position. This process is then repeated again for channel 1 and the bottom solenoid. The firing sequence consists of 7 operations (on, wait, off, wait, on, wait, off), which correspond to the "load" and "fire" positions of figure 4.

2.2 – RPM Sensors

For the purpose of WebLab, it was desired to have a time trace of the wheel motion from which the angular velocity and RPM could be calculated. Each time the wheel passed through a certain position, a signal is sent and recorded to an output file. The remote user can then interpret the data to obtain the desired wheel parameters such as RPM. There exists a wide range of readily available angular motion sensory equipment. The chosen device needed to be water resistant, cost effective, and able to interface with LabView.

When first testing the shooter wheels, it was noticed that most rubber wheels are not symmetric. As the wheels ramp up to speed, the rubber in the wheels expands radialy outward due to the centripetal acceleration. The rubber does not expand equally in all directions causing a shift in the center of gravity of the wheels, in turn creating instabilities. At certain angular velocities the wheels exhibited these instabilities which would shake the experimental setup. It was decided to use an optical sensor so that no parts would touch the wheels during operation and be subjected to this unstable behavior. The wheels were professionally balanced to alleviate most of the instabilities which arose from this asymmetry.

Two ROS-W brand remote optical sensors were chosen from Monarch Instruments that are capable of angular velocities of 0 to 250,000 RPM. Each sensor is made from 303-stainless steel and has dimensions of 2.9 in. long by 0.6 in. in diameter. The range of the sensors is 36 in. The output signal is a TTL style pulse with amplitude equal to the negative of the input voltage.

The light beam from the optical sensor is aimed at the wheel. A piece of reflective tape was placed on the wheel so that it would pass through the light beam once per revolution. As the reflective tape passes through the beam, some of the light is reflected back to the sensor trigging an output pulse equal to the input voltage of 12 Volts DC. This signal is then read by the LabView DAQ card, and a time trace of the wheel's angular motion can be obtained. The two sensors were mounted on the aluminum wheel motor mounting brackets and aimed such that the light beam hit the rubber tire about at about 80% of the wheel radius. The reflective tape was then adhered to that same spot on the tire.

LabView programming for the RPM sensors was straightforward. DAQ Assistant was used to read in the signals from the two sensors. The acquisition rate from the DAQ Assistant was given in the user instructions. With this data a time trace can be plotted and RPM can be readily obtained. A sample plot is shown in figure 2.6 where the wheels were rotating at 80 RPM. Each pulse in this plot represents one revolution where the optical sensor passed the piece of reflective tape adhered to the wheel.

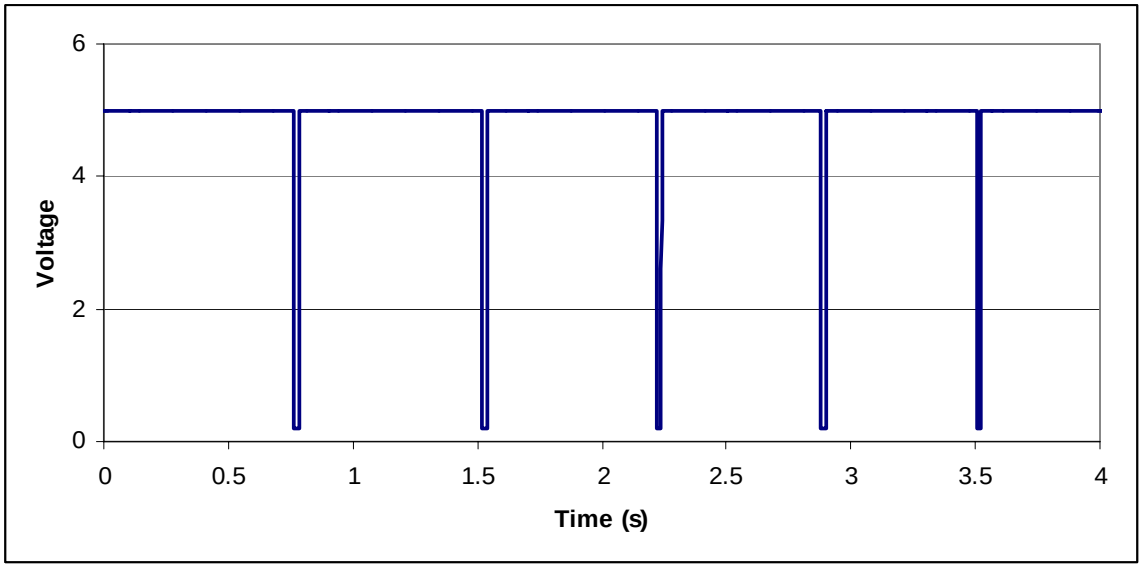

Figure 2.6 – Time trace of wheel angular motion from optical sensors at an angular velocity of 80 RPM. The default value is 5 Volts and the triggered signal is a TTL pulse to 0 Volts.

For the purpose of this thesis, however, it was desired to write a LabView program which would compute the RPM for each run and record it along with other output data. The same DAQ Assistant was used to read in the angular motion data. This data was then put into an array for processing. A counter was created in LabView by creating a feedback loop which would increment by one every time the trace crossed a given threshold voltage. The RPM was then calculated with the end count, acquisition rate and acquisition period (equation 2.1). Such a loop was created for each wheel.

$$RPM = \frac{\#counts * sample\ \ rate}{\#samples} * 60 \qquad [2.1]$$

Final RPM calculations were compared to a hand held optical RPM sensor from Monarch Instruments. Seldom did the two wheels start in the same position when data was acquired. Thus, error was introduced due to the fact that differences in pulse count at a given RPM can be obtained depending on the location of the reflective tag at the beginning and end of the data acquisition period. This was especially apparent at low angular velocities where error in RPM was as much as 10%. This error could be reduced by placing more tags equally spaced along the circumference of each wheel.

2.3 – Break Beam Sensors

In order to obtain the ball speed as it left the shooting mechanism, two break beam style optical sensors were used. It was found that the same ROS-W remote optical sensors used for determining wheel RPM could be used for the break beam application. Again, it was desired that the device be water resistant as the sensors would be close to the path of the falling ball and the corresponding water jet.

Two pieces of plexy glass where bolted to the center of the aluminum frame parallel to the spinning wheels hanging down toward the tank. These where originally intended as a safety precaution in the event that a ball might slip out sideways from the wheel path, but proved an ideal location for the break beams. A set of holes were drilled at increments of 10cm along the center of one plexy glass plate in which the sensors were placed. The sensor was threaded along its body so that jam nuts could be used to hold it in place. Reflective tape was placed at the same 10 cm increments on the opposite plexy glass plate. Figure 2.7 shows the break beam configuration.

The beams were aligned to intersect the decent path of the ball. The beams shined on a piece of reflective tape on the opposite side of the wheels registering 5 Volts. As the falling ball passed through it broke the light beam and the sensor registered 0 Volts. When the ball passed through the beam, the sensor picked up the reflected light beam from the reflective tape and the sensor sent the 5 Volt signal again. The velocity of the projectile is equal to the distance traveled divided by the time required to travel that distance. The time difference between the pulses along with the distance between the two sensors can then be used to determine the average speed between the two sensors (equation 2.2).

$$Average\ \ speed = \frac{beam\ \ dis * sample\ \ rate}{\Delta index} \qquad [2.2]$$

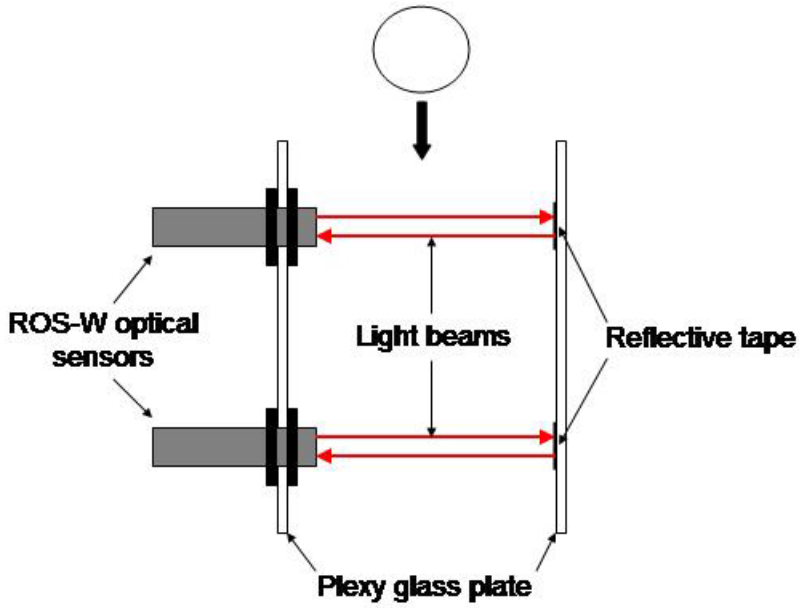

Figure 2.7 – Illustration of break beam configuration. Break beam sensors were used to measure initial velocity of the projectile. The time difference between the pulses along with the distance between the beams was used to calculate the velocity.

The output pulses were read by the LabView DAQ card. LabView programming was done using a very similar method as with the RPM sensor programming. DAQ Assistant was used to read in the signals from the two sensors from two different channels. The acquisition rate from the DAQ Assistant was again given. With this data a time trace can be plotted and ball speed can be readily obtained.

A separate program was written for the purpose of this thesis which would output the speed of the ball for every experimental run. It was noticed that the water jet formed by impact was always vertical. This water jet also tripped the break beams, giving more data then desired. This increased difficulty of programming. A program was written in which the data from each sensor was put into an array. The program would index through the array until the first pulse was found. The corresponding index would then be recorded for the first two pulses and the rest of the data would be disregarded. The difference between the index counts from the two sensors was then calculated. The average ball speed between the two sensors was then found by multiplying the data

acquisition rate by the difference in index counts. This answer was then converted into appropriate units.

Ball speed was also found using the high speed camera by finding the pixel position of the projectile for each frame. Using the frame rate of the camera the time trace of the ball position was found. This position data was then differentiated with respect to time to produce the ball speed. A sample of the data obtained from this method is shown below in figure 2.8 which shows position and velocity data of an impacting 5.72 cm sphere from the moment it was dropped from 30 cm until it reached a depth of about 10 ball diameters. Depth was characterized by the number of ball diameters the sphere was in relation to the free surface, which is denoted by the z = 0 line. Positive z represents air above the interface and negative z represents water.

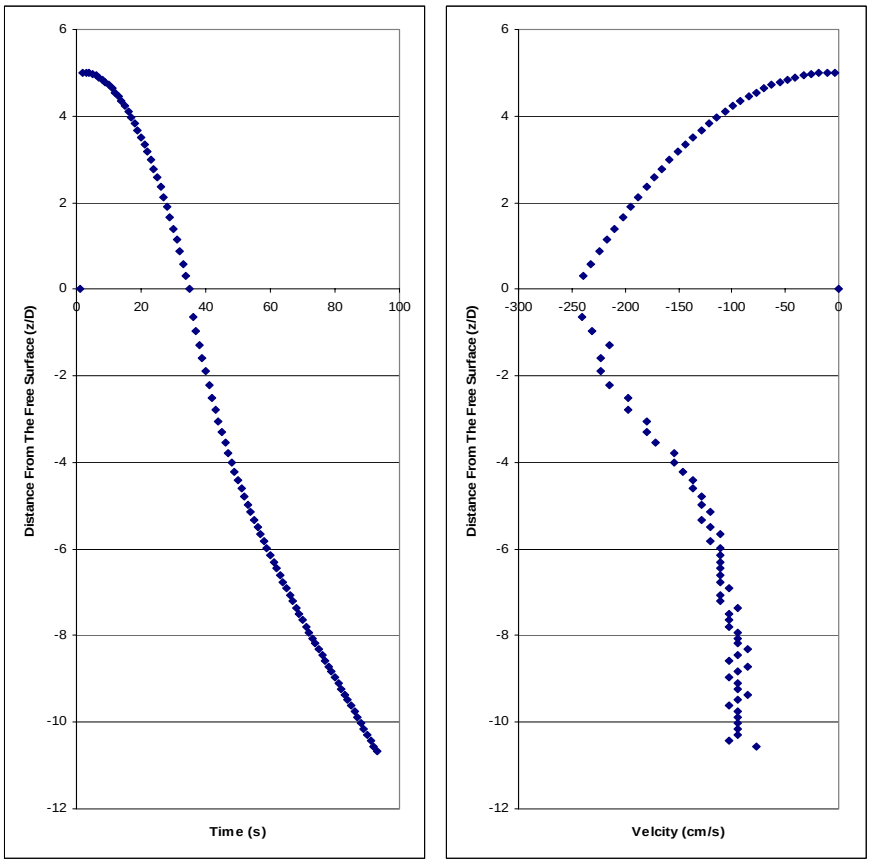

a. b.

Figure 2.8 – Position and velocity data throughout the impacting process for a 5.72 cm sphere being dropped from 30 cm. The free surface is denoted by the z = 0 line. Position data was obtained from high speed imaging techniques and velocity was obtained by taking the derivative of this data.

Free fall tests were performed in air to compare ball speed obtained with the high speed camera with theoretical predictions. It was found that less than 1% error existed between the camera data and theory. Therefore, it was assumed that comparing velocity profiles from high speed imaging to the break beam output was an adequate assessment of the accuracy of the break beams.

The high speed camera was placed and focused such that the field of view covered the distance between the break beams. Any camera lighting close to the reflective tape caused the break beams to not function properly, which in this case proved to be the limiting factor. Thus, compromises were made. The field of view was lowered such that the bottom break beam was just visible. Light beams were aimed lower so the break beams were not affected. The frame rate was also lowered to 314 frames per second, making the given lighting sufficient to acquire dark, but sufficient, images. Camera images and break beam data were taken for 4 tests with RPM ranging from 160 to 1770. Figure 2.9 below shows the velocity comparison between the break beam output data from LabView with the camera data for the same 4 tests.

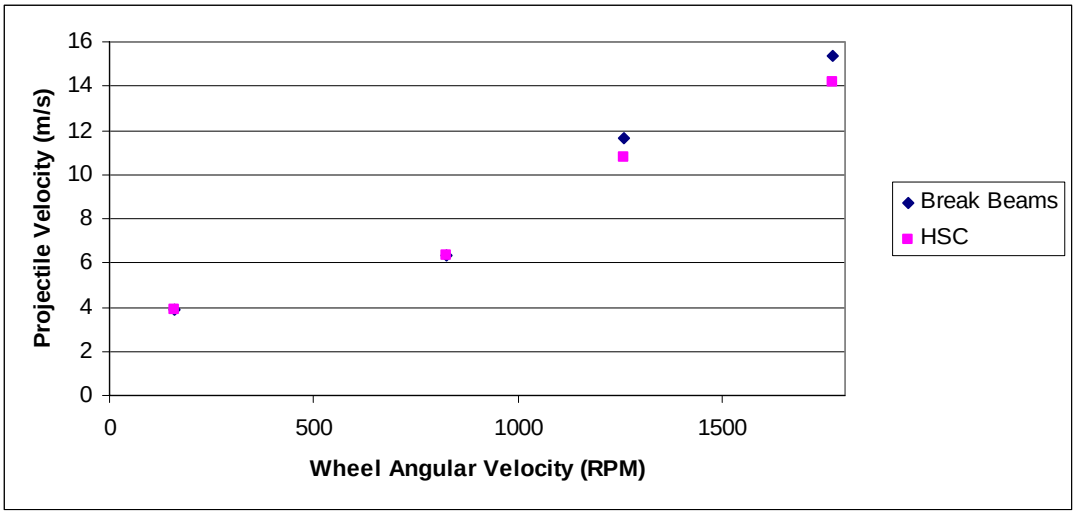

Figure 2.9 – Projectile velocity comparison obtained from break beam sensors and a high speed camera. This test validated the use of break beams for an estimate of the initial projectile velocity.

This data showed that at low speeds the break beam output and the high speed imaging resulted in almost identical ball speeds. At the higher velocities there was a noticeable deviation. It must be mentioned that at higher velocities the camera images were blurry and only contained about 10 images in the field of view. Higher frame rates and better lighting could have been used to correct for this blurriness. It is sufficient to say that this test validated the functionality of the break beams. In all tests prepared for this thesis, higher frame rates were used and the impact velocity was obtained by the images at the time of impact.

2.4 – LabView Programming Logic

Two local computers were used for the operation of the WebLab project. The LabView hardware used for WebLab included:

- 1 PCI-7342 motion control card
- 1 NI-DAQ PCI-MIO-16E-4 data acquisition card
- 1 CB68LPR breakout terminal
- 1 79RCK8 backplane
- 2 60 Volt relays

The motion control and data acquisition cards were installed in one of the local computers. The motion control card was connected to the backplane for the operation of the two solenoids and to the breakout terminal for the operation of the two wheel motors. The data acquisition card was connected to the 68 pin box which was used for the control of the two stepper motors, break beams, RPM sensors, as well as data acquisition.

A dedicated WebLab website was constructed, which controls the operation of the impact laboratory (http://imarine.mit.edu/). Requests to perform an impact experiment are submitted through this site. The input parameters of wheel RPM and angle of impact are entered along with options for instrumentation and data acquisition. The purpose of the LabView program was to read in the input parameters from the remote host computer and then run the impact experiment.

The overall LabView program is a sequence of sub programs contained in a sequence structure. In the first sequence the WebLab computer listens for experimental requests by way of TCP/IP. When an experiment is requested the program reads the input parameters and places them in a queue. Queuing was used in the event another experiment was requested before the first one was completed.

The next sequence contained the program to turn on the wheel motors. The wheel motors require a 0-10 Volt DC input corresponding to wheel speeds of 0 to 1700 RPM. Tests were performed to determine the correlation between voltage and RPM which was found to be linear. This correlation was used in LabView to output the correct voltage from the RPM input. The RPM voltage was then passed to the motion control board, the wheel motor drivers and then to the wheel motors. Actual wheel motor RPM obtained with a Monarch Instruments hand held optical sensor was found to be within 2% of the requested RPM.

As the wheel motors were ramping up to speed the angle of impact parameter was read into the next sequence. It was desired that the ball impact the same place at the surface of the water. This enabled the camera to be stationary and capture the impact location for various angles of impact. A geometric relationship between the angle of impact and horizontal platform location was derived using the release height of the ball over the water. Two Superior Electric stepper motors (model KML091F07) which were each connected to a Superior Electric SLO-SYN (model SS200MDH) translator drive were used to position the platform in the correct angular and horizontal orientation. The stepper motors were also coupled with a 12:1 gear reduction to increase accuracy and torque output. Each pulse to the stepper motors / gear reducer produced a 1/2400 revolution. NI Motion Assistant was used to generate the LabView code for the stepper motors. Input parameters for the stepper motor program include steps/sec, acceleration, jerk, and number of steps. The optimum angular velocity, acceleration and jerk were made constant throughout the program and the number of steps was made an input. Number of steps for the two stepper motors was coupled by the geometric relationship which was in turn governed by the angle of impact parameter.

The program then goes through a wait period of 2 seconds to allow for any motion from the start up of the motors or from the positioning of the platform to stop. During the wait period RPM data is acquired. The firing sequence described in section 2.0 was then initiated. The firing sequence also acted as a trigger for the acquisition of high speed camera images, wave probe and break beam data. Once triggered, data was acquired for a determined time for each device. For most shots, the high speed camera saves data for 2 seconds at a frame rate of 600 frames per second. Wave probe and break beam data is saved for 5 and 2 seconds respectively. All of the data acquired during the program was then saved to a location on the host computer which can be downloaded by the remote user.

The next two sequences stopped the wheel motors and moved the platform back to the default zero degree position. In the program used for this thesis additional sequences were added to perform the calculations on the RPM and break beam data described previously. The final answers for RPM of each wheel and ball speed were saved in the same folder as the other data. The last sequence sent an e-mail to the user reporting a successful experimental run and informed the user of the location of their saved data.

2.5–Final Experimental Setup

The completed WebLab experimental setup consisting of the loader, shooter and tank is shown in Figure 2.10. Other experiments performed for this thesis required various sized spheres. For such experiments a 0.6 m x 1.2 m x 0.9 m aquarium was used in place of the main tank. This allowed for easier retrieval of the smaller spheres. During drop tests, an electro magnet was used to release the steel balls. The electromagnet was mounted on a plastic bar which could be raised and lowered depending on the desired impact velocity. This apparatus is shown in figure 2.11.

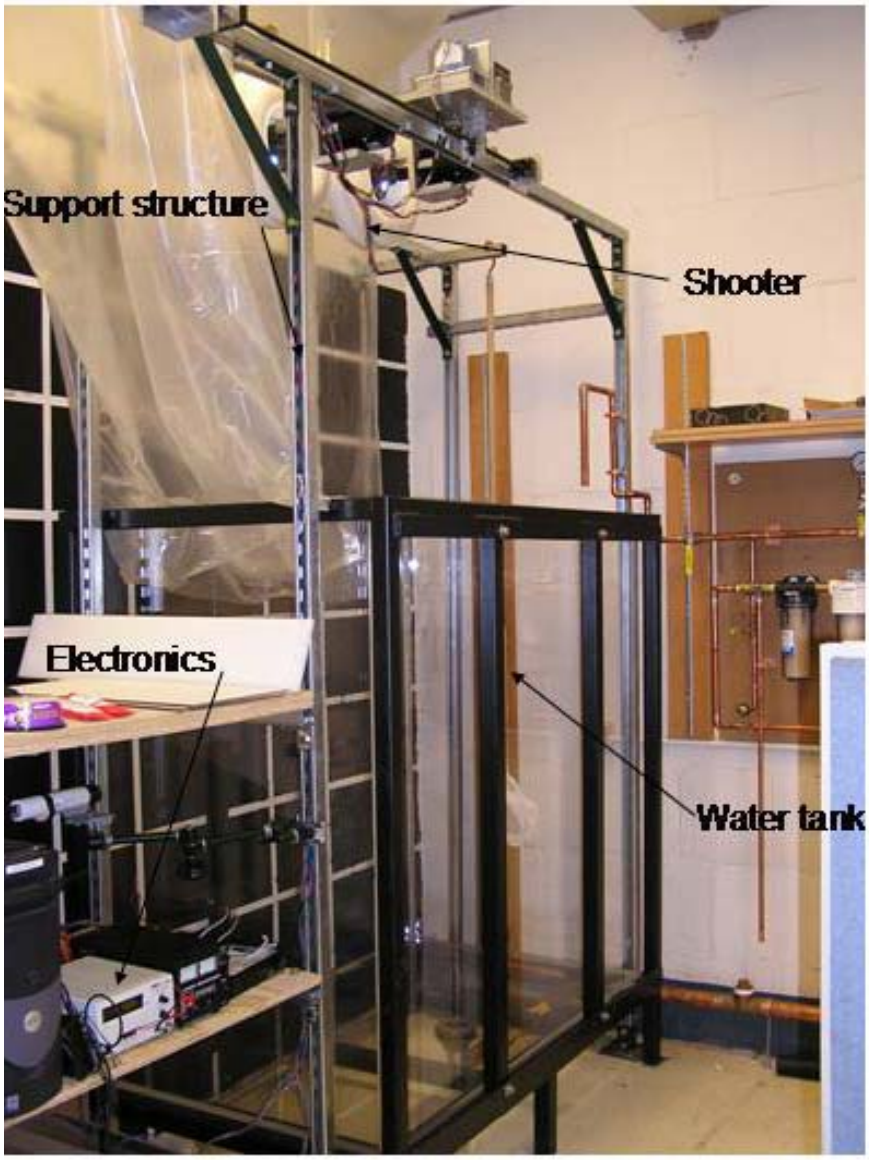

Figure 2.10 – WebLab experimental setup used for the experiments contained in this thesis. A high speed camera and halogen lights were aimed at the center of the tank to obtain images.

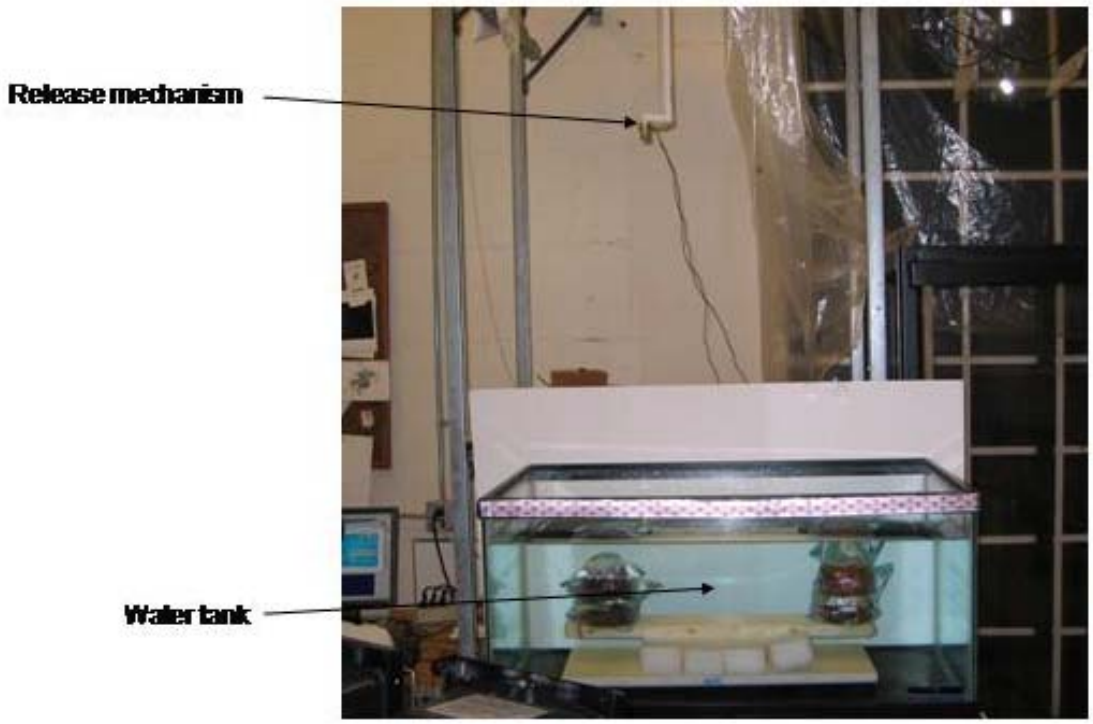

Figure 2.11 – Drop test experimental setup. The release mechanism holds the spheres and drops them upon command into the water tank. A high speed camera captures the impact event.

Chapter 3

Impact Coefficients

3.0 – Theory

Numerous experiments have been performed in order to characterize splash and impact. The first to study such phenomena were Von-Karman and Wagner in order to find the forces exerted on a sea plane float during landing [19 &20]. The non-dimensional parameter which governs impact force is the impact, or slamming coefficient, which is defined as:

$$C_s = \frac{F_I}{\frac{1}{2}\rho V^2 A_x}, \qquad [3.1]$$

where F_I is the impact force, ρ is the density of the fluid, V is the impact velocity, and A_x is the projected area of the object.

The balls used in this experiment are denser than water and thus the change in velocity during the data acquisition period (of ½ ball diameter) is negligible for the range of impact velocities tested. The velocity is thus considered constant throughout the impact entry period. This is consistent with results obtained by image processing. A zero

change in velocity translates into zero deceleration; thus no impact force arises during the first moments of impact. It is obvious however, that there is indeed a force since fluid is violently displaced around the sphere during impact. However, this force is not sufficient to decelerate the ball during the small time it takes for the ball to reach a depth of ½ sphere diameter. A closer look at the physics of the problem offers insight into the force at impact.

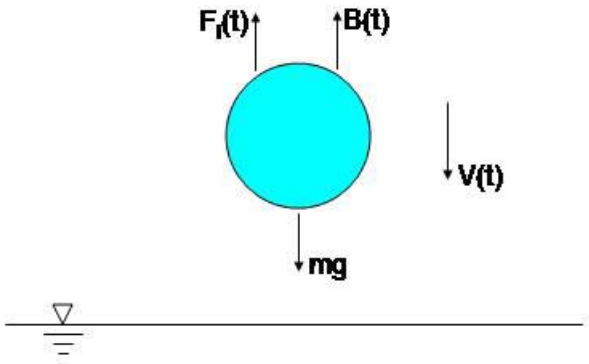

Figure 3.1 – Theoretical water impact problem statement. A rigid sphere with mass *m* impacts the free surface with velocity *V*.

Consider a solid sphere impacting the free surface with velocity, *V* (figure 3.1), where $F_I(t)$ is the impact force, $B(t)$ is the buoyancy force, and mg represents the gravity force on the sphere. From Newton's second law:

$$\sum F = ma \qquad [3.2]$$

$$mg - B(t) - F_I(t) = \frac{d}{dt}\left[mV(t)\right] \qquad [3.3]$$

Using conservation of momentum, the velocity can be expressed as:

$$V(t) = \frac{mV_o}{m + m_a(t)} \qquad [3.4]$$

Where m and m_a are the mass and added mass of the sphere respectively. Substituting equation 3.4 into equation 3.3 yields:

$$F_I(t) = mg - B(t) - mV_o \frac{d}{dt}\frac{m}{m + m_a(t)} \quad [3.5]$$

$$F_I(t) = mg - B(t) + m^2 V_o \frac{\dot{m}_a}{\left(m + m_a(t)\right)^2} \quad [3.6]$$

$$F_I(t) = mg - B(t) + \left(\frac{m}{m + m_a(t)}\right)^2 \left(\dot{m}_a(t) V_o\right) \quad [3.7]$$

Because the phenomena of interest occurs during the first moments of impact where the sphere has at most ½ diameter immersion, it can be assumed that $m_a << m$. After ½ diameter, cavities form and the boundary conditions no longer hold. In which case equation 3.7 reduces to:

$$F_I(t) = mg - B(t) + \left(\dot{m}_a(t) V_o\right) \quad [3.8]$$

From the above equation the impact force can be evaluated. It is noticed that the buoyancy force and the time rate of change in added mass is a function only of geometry, in particular, the instantaneous immersed volume. The immersed volume of a sphere of radius R as a function of depth, $D(t)$ is:

$$\forall(t) = \pi R\left(D(t)\right)^2 - \tfrac{1}{3}\pi\left(D(t)\right)^3 \quad [3.9]$$

The buoyancy force is equal to the mass of the displaced liquid:

$$B(t) = \rho g \forall(t) \quad [3.10]$$

Substituting equation 3.9 into the above equation yields an equation for the buoyancy force as a function of immersion depth:

$$B(t) = \rho g\left[\pi R\left(D(t)\right)^2 - \tfrac{1}{3}\pi\left(D(t)\right)^3\right] \qquad [3.11]$$

The added mass is found from a method used by Miloh [12, 13]. A brief overview of his derivation is presented here. The boundary value problem for the velocity potential $\phi(r,z,t)$ in spherical coordinates is governed by:

$$\nabla^2\phi = 0 \qquad z \geq 0 \qquad [3.12]$$

with body and free surface boundary conditions:

$$\begin{aligned} &\frac{\partial\phi}{\partial n} = \overline{V}\bullet\overline{n} && on \quad S \\ &\phi = 0 && z = 0 \\ &\phi \longrightarrow 0 && r^2 + z^2 \longrightarrow 0 \end{aligned} \qquad [3.13]$$

The origin of the coordinate system is at the free surface with positive *z* pointing downward. *S* is the sphere's boundary and $\overline{n}$ is the normal vector pointing outward from the surface of the sphere. Wagner used this same approach with the difference being that he simplified the governing equations by substituting the flat plate approximation for the more complex spherical boundary. That is why this approach is known as the Generalized-Wagner Method. This approach was also used to derive a Generalized-Wagner impact coefficient presented later on in this paper. The kinetic energy of the surrounding fluid can be written as:

$$\begin{aligned} T(\theta_0) = \tfrac{2}{3}\pi\rho a^3 V^2 \int_0^\infty \left(4p^2+1\right)\frac{\cosh\left(p\left(\pi-\theta_0\right)\right)}{\sinh\left(2p\pi\right)\cosh p\theta_0} * \\ \left[3\sinh p\theta_0 \cosh p\left(\pi-\theta_0\right) - \cosh p\theta_0 \sinh p\left(\pi-\theta_0\right)\right] dp \end{aligned} \qquad [3.14]$$

The parameter $\theta_o(t)$ in the above equation represents the instantaneous angle of the sphere below the free surface as shown below in figure 3.2.

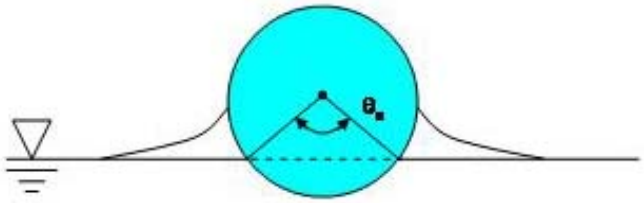

Figure 3.2 – θ_o is defined as the angle between the water sphere interfaces. This quantity is a function of time and is used in kinetic energy calculations.

It is also noted from conservation of energy that fluid kinetic energy is related to the added mass, m_a of the object by the following equation:

$$\tfrac{1}{2} m_a V^2 = T\left(\theta_o\right) \qquad [3.15]$$

Equation 3.12 was then solved by considering the small-time expansion of the fluid kinetic energy of equation 3.14. The kinetic energy can also be written in terms of τ and a small parameter ε as:

$$T\left(\varepsilon\right) = \tfrac{4}{3}\rho R^3 V^2 \varepsilon^2 \left(1 - 0.35\varepsilon - 0.17\varepsilon^2\right) + 0\left(\varepsilon^6\right) \qquad [3.16]$$

where,

$$\tau = \frac{b(t)}{R} = \frac{Vt}{R} = \frac{\varepsilon^2}{2} + 0\left(\varepsilon^3\right) \qquad [3.17]$$

$$\varepsilon\left(\tau\right) = \pi - \theta_0\left(\tau\right) \qquad [3.18]$$

Equation 3.14 implies that the added mass coefficient $\lambda(\tau)$ of a double spherical bowl of semi-axis b, with $b=V$, is given by:

$$\lambda(\tau) = \frac{2T}{\pi\rho R^3 V^2} = \frac{16\sqrt{2}}{3\pi}\tau^{\frac{3}{2}} - 1.19\tau^2 - 0.837\tau^{\frac{5}{2}} + 0\left(\tau^3\right) \qquad [3.19]$$

The added mass coefficient of a half spherical bowl, such as the bottom of the sphere in the performed experiments is half of equation 3.19. The added mass of the projectile after ignoring higher order terms is then:

$$m_a(t) = \tfrac{1}{2}\lambda(\tau)\pi\rho R^3 \qquad [3.20]$$

$$m_a(t) = \tfrac{1}{2}\left[\frac{16\sqrt{2}}{3\pi}\tau^{\frac{3}{2}} - 1.19\tau^2 - 0.837\tau^{\frac{5}{2}}\right]\pi\rho R^3 \qquad [3.21]$$

$$m_a(t) = \tfrac{1}{2}\left[\frac{16\sqrt{2}}{3\pi}\left(\frac{Vt}{R}\right)^{\frac{3}{2}} - 1.19\left(\frac{Vt}{R}\right)^2 - 0.837\left(\frac{Vt}{R}\right)^{\frac{5}{2}}\right]\pi\rho R^3 \qquad [3.22]$$

It is noticed that the assumption made to reduce equation 3.7 is here verified. The added mass is much less than the mass of the sphere for the small impact time duration used for this experiment.

Taking the time derivative of equation 3.22 and simplifying yields the desired time rate of change in added mass:

$$\dot{m}_a(t) = \tfrac{1}{2}\pi\rho V R^2\left[\frac{8\sqrt{2}}{\pi}\tau^{\frac{1}{2}} - 1.19\tau - 0.837\tau^{\frac{3}{2}}\right] \qquad [3.23]$$

The impact coefficient can now be found by substituting equations 3.7, 3.11 and 3.23 into equation 3.1 and simplifying yields:

$$C_s(t) = \frac{F_I(t)}{\frac{1}{2}\rho V^2 A_x} \qquad [3.24]$$

$$C_s(t) = \frac{mg - B(t) + \left(\dot{m}_a(t)V_o\right)}{\frac{1}{2}\rho V^2 A_x} \qquad [3.25]$$

$$C_s(t) = \frac{mg - \rho g\left[\pi R\left(D(t)\right)^2 - \frac{1}{3}\pi\left(D(t)\right)^3\right] + \frac{1}{2}\pi\rho V^2 R^2\left[\frac{8\sqrt{2}}{\pi}\tau^{\frac{1}{2}} - 2.38\tau - 2.0925\tau^{\frac{3}{2}}\right]}{\frac{1}{2}\pi\rho V^2 R^2} \quad [3.26]$$

This slamming coefficient assumes that the free surface is flat during the impact process. In reality the free surface deforms a height ξ* around the sphere upon impact as seen below in figures 3.3 and 3.4.

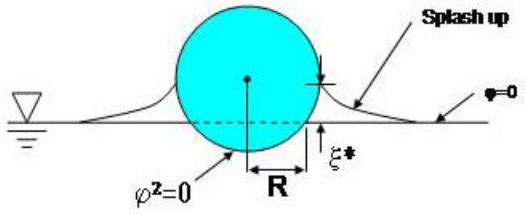

Figure 3.3 – Surface deformation caused by impact.

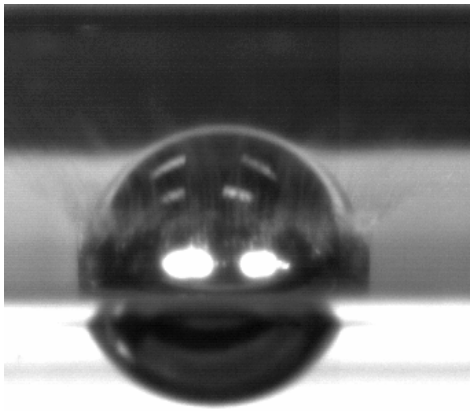

Figure 3.4 – Image of the surface deformation caused by a sphere impacting the free surface at 3.8 m/s. The water rides up around the sphere and the free surface can not be considered flat throughout the impact process.

Correction must be made for the free-surface deflection around the sphere during impact. Miloh introduces a correcting surface wetting factor, C_w which for a sphere is:

$$C_w = 1.327 - 0.154\tau \quad [3.27]$$

This in effect raises the free surface by the amount ξ^*. Thus, the ball submergence, b should be replaced by b^* such that:

$$b^*(t) = b(t) + \xi^*(t) \qquad [3.28]$$

The instantaneous submergence depth, b in the kinetic energy and added mass equations should be replaced by this corrected submergence depth b^*. The corrected slamming coefficient is then:

$$C_s(t) = \frac{mg - \rho g\left[\pi R C_w^2 \left(D(t)\right)^2 - \frac{1}{3}\pi C_w^3 \left(D(t)\right)^3\right]}{\frac{1}{2}\pi\rho V^2 R^2} + \frac{\frac{1}{2}\pi\rho V^2 R^2\left[\frac{8\sqrt{2}}{\pi} C_w^{\frac{3}{2}}\tau^{\frac{1}{2}} - 2.38 C_w^2\tau - 2.0925 C_w^{\frac{5}{2}}\tau^{\frac{3}{2}}\right]}{\frac{1}{2}\pi\rho V^2 R^2} \qquad [3.29]$$

Von-Karman derived a theoretical expression for the impact coefficient of a falling sphere in 1929 [19] using a similar approach as Miloh. However, the added mass coefficient was found using flat plate approximations instead of using the more complex spherical equations. The added mass of a flat plate is simply:

$$m_{a\ Plate} = \rho\tfrac{2}{3}\pi R^3, \qquad [3.30]$$

where R is the instantaneous half length of the flat plate taken at the undisturbed free surface, as seen below in figure 3.5.

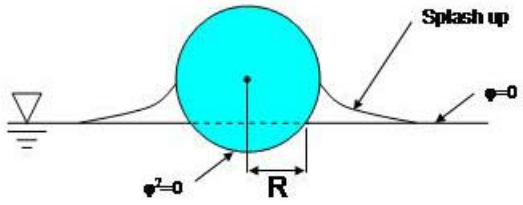

Figure 3.5 – Von-Karman impact coefficient setup. Von-Karman considered the free surface flat during the impact process while in reality water rides up along the sphere.

Von-Karman does not take into account the deformation of the free surface around the outside of the sphere. His derivation assumed the free surface to be flat and stationary throughout the impact process. This represents a surface wetting factor, C_w of unity. The resulting Von-Karman estimate for the impact coefficient is then:

$$C_s = 3.30\tau^{3/2} \qquad [3.31]$$

In 1932, Wagner [20] used the same method as Von-Karman to derive another impact coefficient which would take into account the deformation of the free surface. The same flat plate assumption for the added mass coefficient was used as in the Von-Karman model. The main difference between the two models is that Wagner used the distance between the center of the sphere and the top of the meniscus of the surface deformation for the instantaneous half length of the flat plate. This can be seen below in figure 3.6.

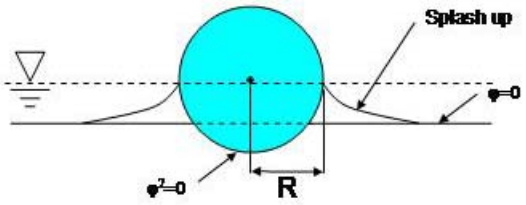

Figure 3.6 – Wagner impact coefficient setup. Wagner took splash up into account by raising the virtual free surface to the top of the surface deformation. However, he still considered the surface to be flat throughout the impact process.

In Wagner's derivation, he took into account the deformation of the free surface by simply moving the free surface higher. This represents a surface wetting factor, C_w of 1.5. Wagner still held the assumption of an undisturbed free surface. This resulted in a higher estimate for the two-dimensional impact coefficient than Von-Karman. The resulting Wagner estimate for the impact coefficient is:

$$C_s = 6.03\tau^{3/2} \qquad [3.32]$$

A continuation of the derivation used by Miloh to obtain the time varying added mass results in an impact coefficient known as the Generalized Wagner impact coefficient. The penetration depth, *b* and its derivative with respect to time, $\dot{b}$ can be used in the general Krichhoff-Lagrange equations to yield the vertical hydrodynamic slamming force:

$$F_I = \frac{d}{dt}\left(\frac{\partial T}{\partial \dot{b}}\right) - \left(\frac{\partial T}{\partial b}\right) \qquad [3.33]$$

The same surface wetting factor in equation 3.27 is used here again. The kinetic energy of the surrounding fluid found in equation 3.14 can then be substituted into equation 3.33 to yield the Generalized Wagner slamming coefficient for constant velocity water entry:

$$C_s(\tau) = \frac{8\sqrt{2}}{\pi} C_w^{\frac{3}{2}} \tau^{\frac{1}{2}} - 2.38 C_w^2 \tau - 2.09 C_w^{\frac{5}{2}} \tau^{\frac{3}{2}} \qquad [3.34]$$

Equation 3.29 was used to determine the experimental impact coefficient for each of the experimental runs. The results were then compared to the Von-Karman, Wagner, and the generalized Wagner impact coefficients found in equations 3.31, 3.32, and 3.34.

Another way to calculate the force using the high speed camera would be to use a less dense sphere. This would cause the sphere to decelerate at a faster rate. The changes in the velocities would then be captured on the high speed camera and the deceleration could then be found. A wireless accelerometer could also be inserted into the sphere which would record the instantaneous accelerations as a function of time.

3.1 – Set Up

It was decided to perform 9 series of tests ranging in impact speed from 4.8 m/s to 18.3 m/s. Each test was repeated 3 times to test repeatability. The methods described above studied the first moments of water impact where at most ½ of the ball diameter has broken the free surface. Decreasing the field of view increased the maximum frame rate of the high speed camera. It was desired that the field of view include 1 ball diameter above and below the free surface. This would allow for several frames above the free surface for calculation of the impact velocity. For each of the experiments, an 85mm Nikon lens was used. This decreased field of view resulted in a maximum frame rate of 1500 frames per second. An example of the captured images is shown below in figure 3.7.

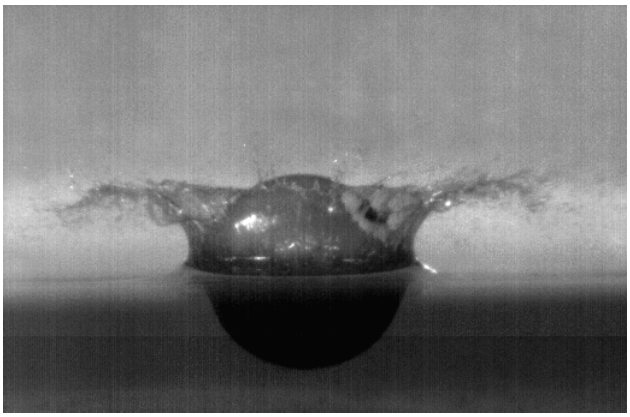

Figure 3.7 – Example of the images acquired during testing. This image was taken of a sphere impacting on the free surface with an impact velocity of 4.8 m/s.

Balls were fired into the water at wheel RPM ranging from 0 to 1700. Velocities were obtained by differentiating the position data directly above the water surface. The bottom of the ball was used as the reference as it entered the field of view. It was also noted that the water caused image distortion at the water interface. Thus, the top of the sphere was used as a frame of reference once the ball entered the water and then offset by the ball's pixel height in air to compensate for the change in reference. For each frame of each experiment the pixel location of the ball was found and recorded. Conversion from pixle coordinate to a length scale was done using the ball as a frame of reference. Billiard balls, such as the ones used in this experiment, have an outside diameter of 5.72 cm (2.25 in). During each run, the pixel height of the ball was found and pixel length was

recorded using the ball diameter. In this manner the ball position was found as a function of the frame. The inverse of the frame rate was then used to convert the frame number to time. The water surface impact location was taken as the origin. The result was position data of the sphere as a function of time.

It was first attempted to use LabView's image recognition software to automate the process of obtaining ball position for each frame. It became tedious to manually find the balls location frame by frame for each experiment. LabView code was written to detect the edge of the ball as it passed through the field of view and then record the position for each frame. The LabView interface is shown below in figure 3.8

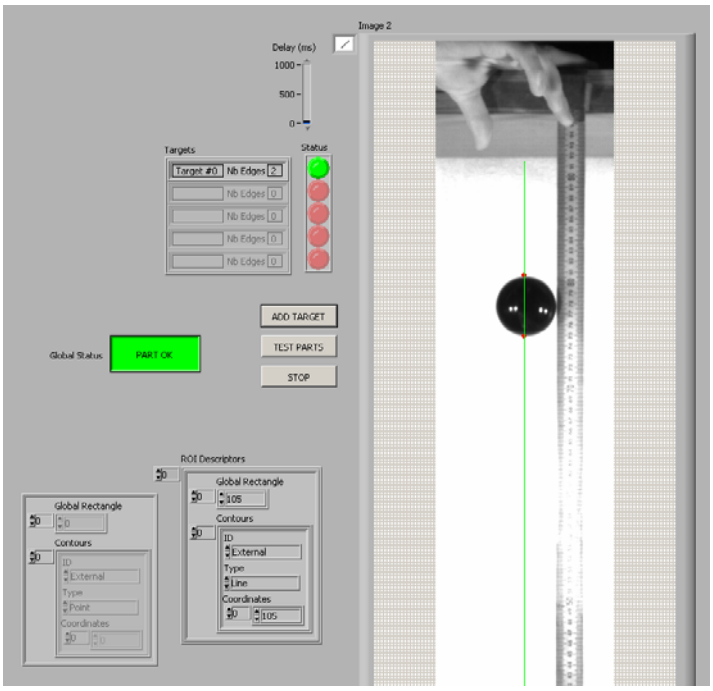

Figure 3.8 – LabView edge detection interface. A black ball on a white background was used with extensive lighting to produce a sharp image. Even under these ideal conditions, the edge detection program did not produce the desired accuracy.

Preliminary edge detection testing was performed in air with a black ball on a white background. Extensive lighting was also used. This allowed for a sharp contrast, low exposure times and a sharp image. Even under these ideal conditions, errors were introduced. It was found that when the ball fell through the air, the edge detection program did find and record the balls position but was not capable of the desired

accuracy for this application. Due to the small time steps involved in high speed photography, any pixel variation between frames will result in large velocity errors which are then magnified in the acceleration calculations. It was noticed that the edge detection program was off by as much as 3 pixels as the spheres passed through air. It must be mentioned that in most applications this is more than sufficient, but for the purpose of this thesis, greater accuracy was desired. In addition, once the ball entered the water, the splash cavity and surrounding surface deformation created other edges which were picked up by LabView edge detection program. Thus, the only time the image recognition program could have been used, even for a preliminary estimate, was prior to impact. Figures 3.9 and 3.10 show velocity vs. time and acceleration vs. time data for a free falling sphere obtained using LabView's edge detection program and compares it with data obtained manually.

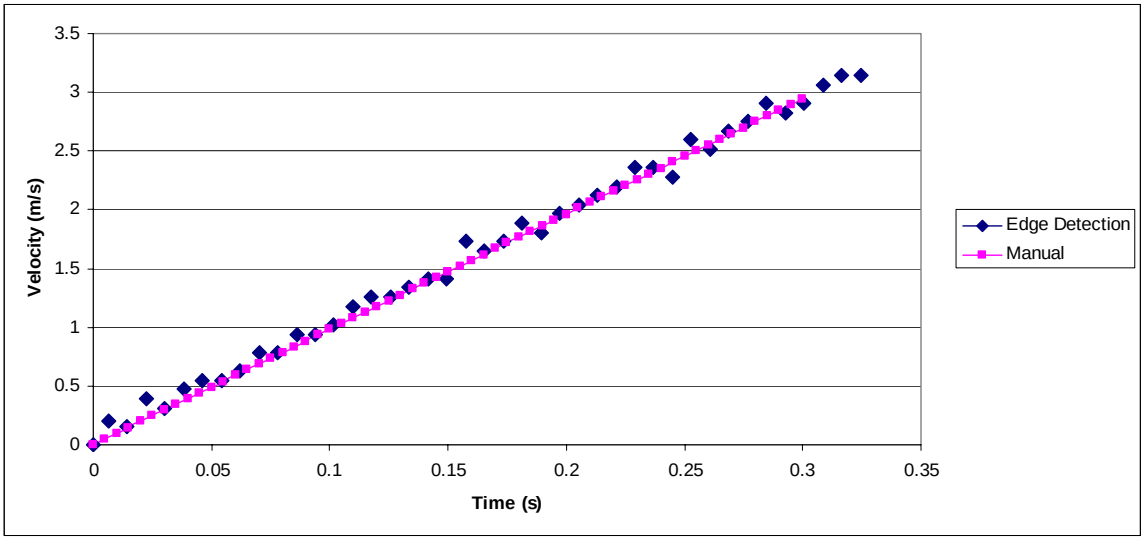

Figure 3.9 – Velocity data of a free falling sphere obtained with a LabView edge detection program compared with manual calculations. The edge detection program resulted in relatively small velocity errors.

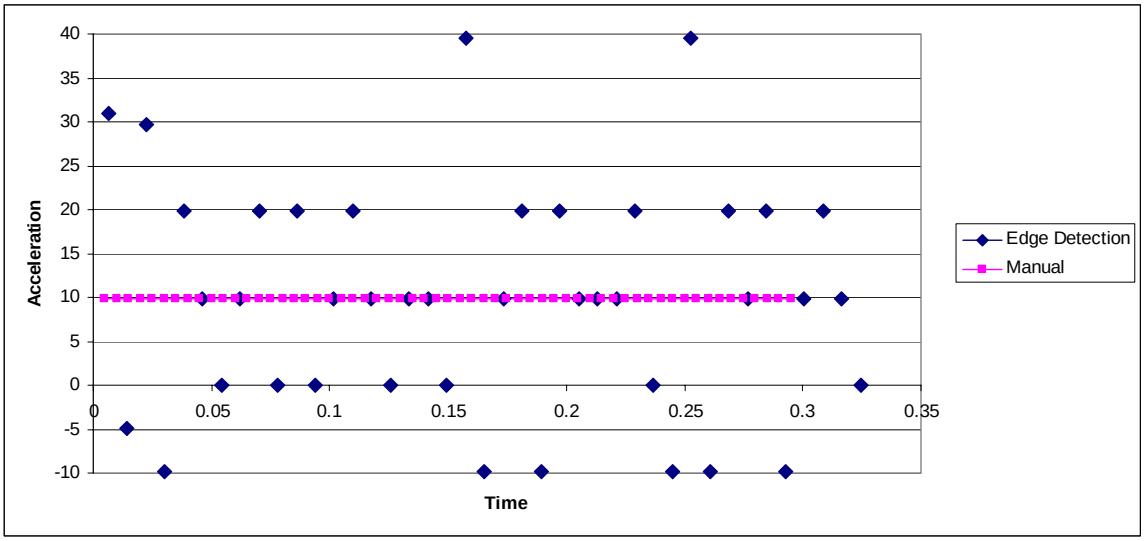

Figure 3.10 – Acceleration data of a free falling sphere. The LabView edge detection position data was differentiated and then compared to the differentiated manual position data. Large errors resulted from small velocity differences due to the small time steps involved.

The velocity data obtained by the edge detection program serves as a good first estimate, but other methods must be used to increase accuracy. Filters could be applied to the position data to smooth out the curves to improve estimates. However, the water entry data of interest for this thesis was simply too unpredictable to be able to apply edge detection techniques. Thus, manual methods were used to obtain all data presented in this thesis.

3.2 – Results

The obtained position data from each of the experimental runs was plotted in Excel and then differentiated to obtain the velocity. At the beginning of this thesis it was assumed that velocity would be constant during the initial stages of impact. Figure 3.11 plots the velocity during the data acquisition period of roughly two ball diameters. The vertical line represents the moment of impact. The discontinuities shown indicate a one pixel difference which demonstrates the need for high resolution and accuracy. Plots for each test demonstrate the same constant velocity trend throughout the impact region of interest. This is consistent with expected results for an impact problem driven by the inertia of the projectile.

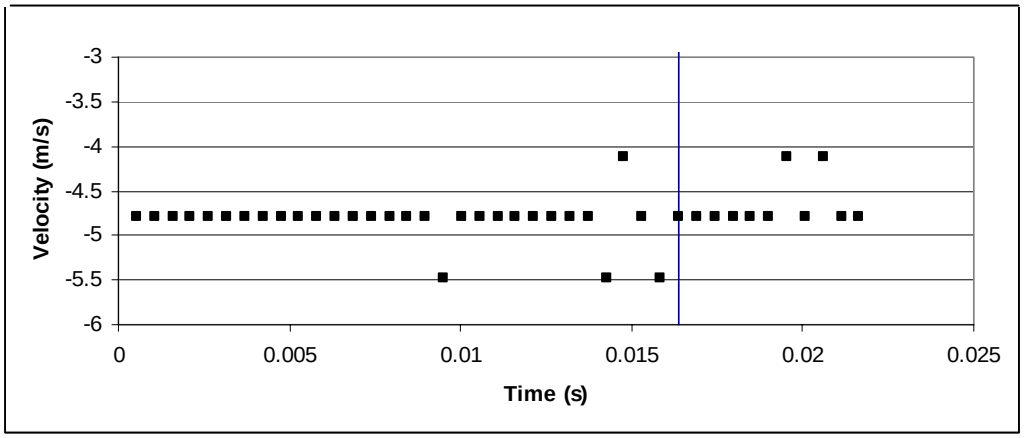

Figure 3.11 – Constant velocity validation for an impact speed of 4.8 m/s. The vertical line shows the moment of impact. The assumptions made in the derivation of the impact coefficient equations are here validated.

Pictures of the initial splash formation were compared for each of the tested impact velocities. Figure 3.12 shows the ball at roughly ½ its ball diameter for each impact velocity. These frames also represent each tests final data point. It can be seen that the water sheet that forms around the sphere at impact decreases in thickness as the impact velocity increases. It is also noticed that the general shape of the splash sheet is the same at each impact velocity. The top of each splash sheet is for the most part horizontal.

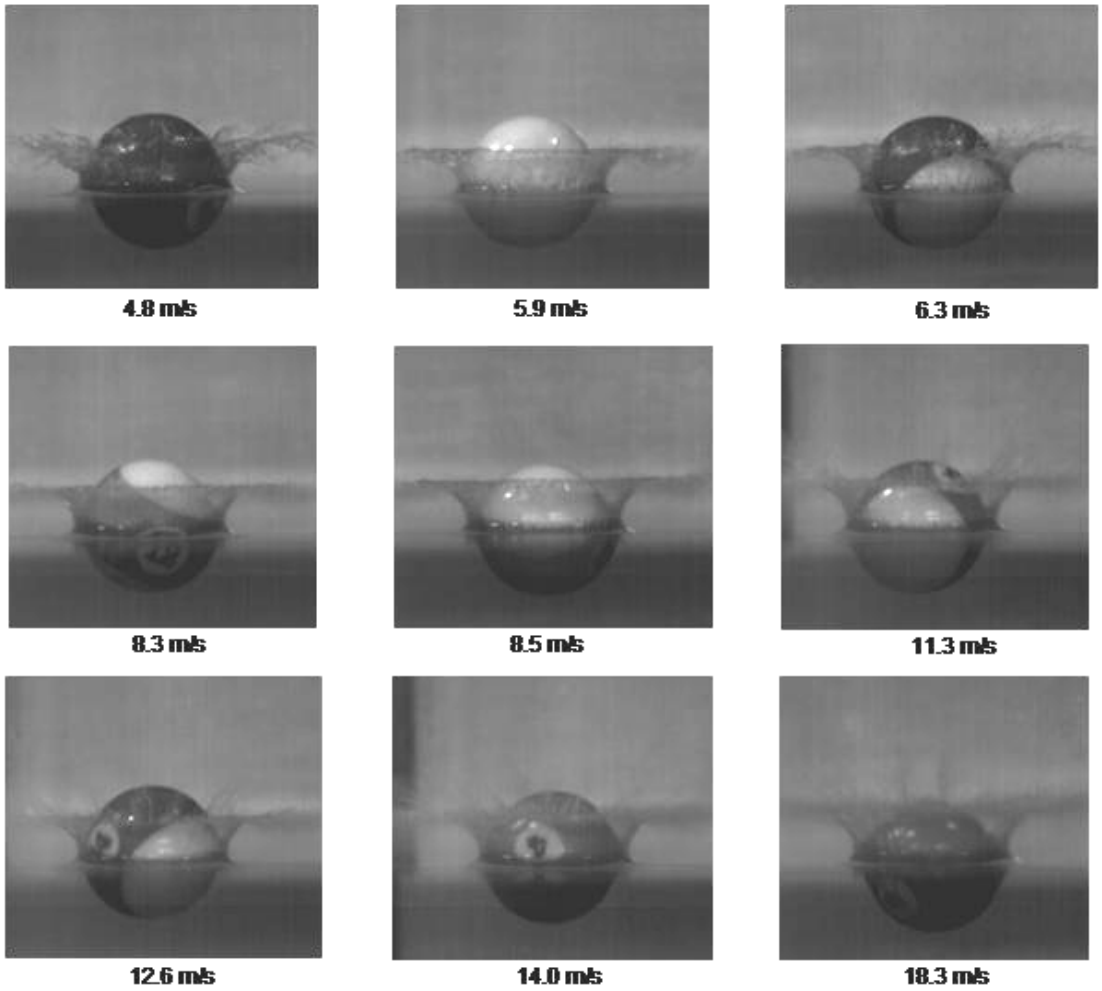

Figure 3.12 – Images at impact over the range of impact velocities tested. The shape of the splash sheet is the same and the top of the sheet is horizontal at each speed.

All of the obtained data was then inserted into equations 3.29, 3.31, 3.32, and 3.34 for the Experimental, Von-Karman, Wagner, and Generalized Wagerner impact coefficients respectively and then plotted for each of the impact velocities. The two following figures show a comparison of the three methods with experimental data for two impact velocities. Figure 3.13 shows the results for an impact speed of 4.8 m/s while figure 3.14 shows results for an impact speed of 14.0 m/s.

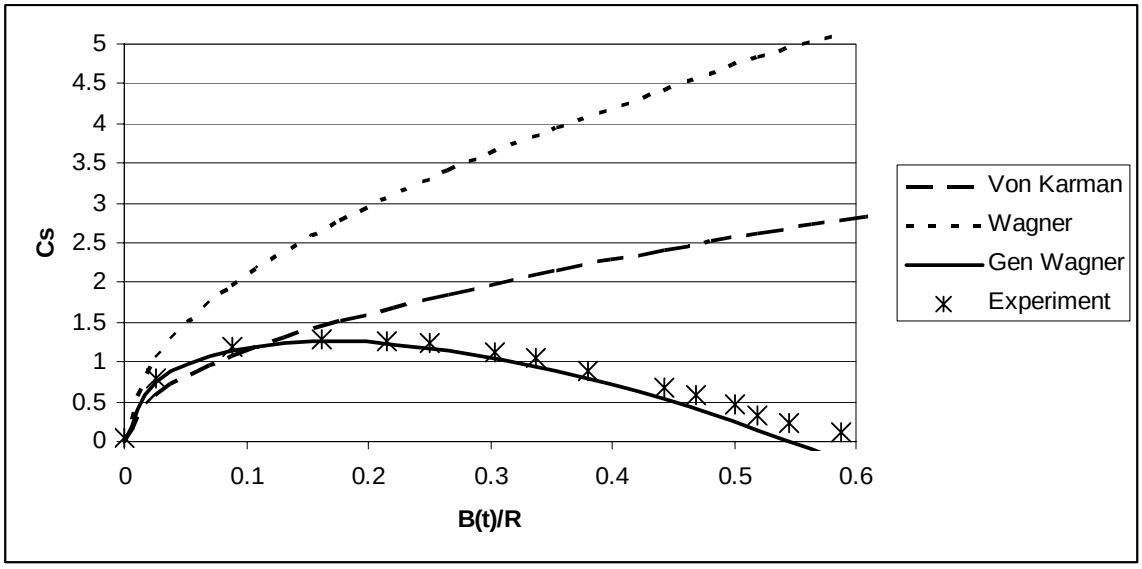

Figure 3.13 – Comparison of impact coefficients for an impact speed of 4.8 m/s. The experimental data follows the Generalized Wagner theory during the initial stages of impact but deviates slightly at higher values of dimensionless depth.

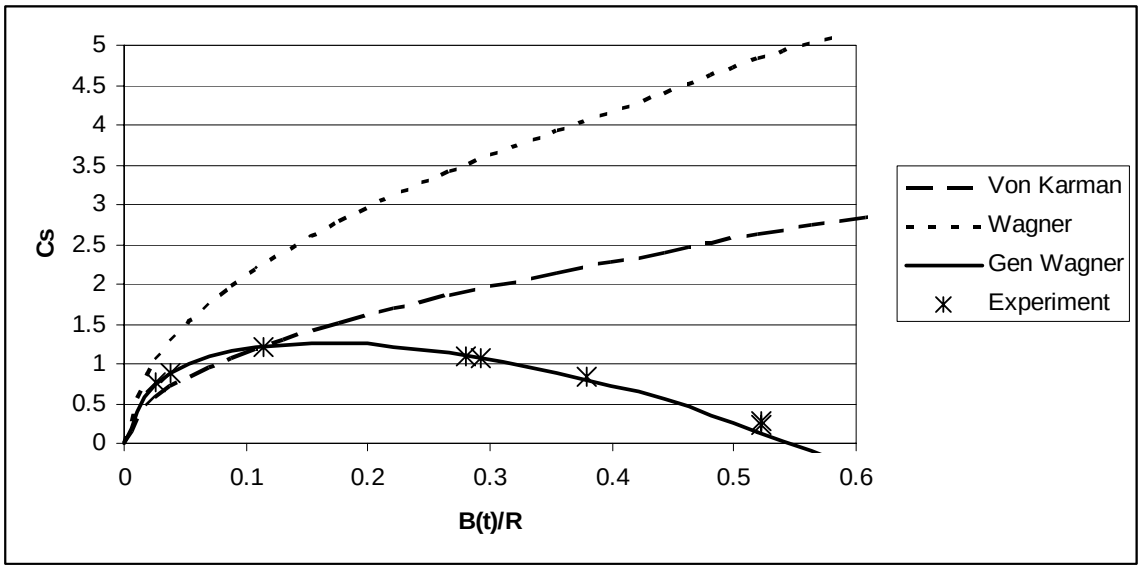

Figure 3.14 – Comparison of impact coefficients for an impact speed of 14.0 m/s. At this higher impact velocity the Generalized Wagner theory gave a good approximation of the experimental data.

As can be seen in the above graphs, the experimental data matches closely with the Generalized Wagner theory. During the initial stages of impact, the Von-Karman impact coefficient underestimated experimental results. This was due in part by the fact that the free surface is not undisturbed during impact and corrections must be taken into account

for an accurate assessment of the impact force. The Wagner theory overestimated experimental results. This was due in most part to Wagner raising the effective free surface to high which yielded higher results. As the immersion depth increased, the Von-Karman and Wagner theories deviated from experimental results. Both Von-Karman and Wagner used flat plate approximations for the impact model and did not take into account the 3-dimensional effects of a spherical body.

As the impact speeds increased, the experimental data tended to more closely follow the Generalized Wagner theory. A closer comparison between the Generalized Wagner and the experimental equation (equations 3.34 and 3.29) for the impact coefficients reveals an interesting result. The first term in equation 3.29 shows that the difference between the two impact coefficients is the addition of the mass and buoyancy terms. This term is shown below in equation 3.35.

$$\frac{mg-\rho g\left[\pi RC_w^2\left(D(t)\right)^2-\frac{1}{3}\pi C_w^3\left(D(t)\right)^3\right]}{\frac{1}{2}\pi\rho V^2R^2} \qquad [3.35]$$

The maximum deviation of experimental data from the General Wagner theory occurred at the higher values of $B(t)/R$ (between 0.4 and 0.5) where *B(t)* is the instantaneous immergence depth. Consider a value of $B(t)/R$ equal to 0.5 (see figure 3.13). This corresponds to a quarter immersed sphere, which is the maximum depth for which the Generalized Wagner equation holds. For a standard pool ball of diameter 5.72 cm, weight 5.9 oz and a maximum value of C_w of 1.327[12], the maximum buoyancy force is equal to 0.25 Newtons. The mass force of the pool ball is 1.64 Newtons. The maximum buoyancy force is then roughly 15% of the mass force. Incorporating this into equation 3.35, the experimental impact coefficient equation can be reduced to:

$$C_s(t) = \frac{0.85mg + \frac{1}{2}\pi\rho V^2 R^2 \left[\frac{8\sqrt{2}}{\pi} C_w^{\frac{3}{2}} \tau^{\frac{1}{2}} - 2.38 C_w^2 \tau - 2.0925 C_w^{\frac{5}{2}} \tau^{\frac{3}{2}} \right]}{\frac{1}{2}\pi\rho V^2 R^2} \qquad [3.36]$$

As the velocity increases the combined mass and buoyancy force has less of an influence on the impact coefficient in the above equation. Thus, the experimental impact coefficient reduces to that of the Generalized Wagner theory. As τ increases, the Wagner term decreases and the constant mass force becomes more prevalent, thus causing a deviation from the General Wagner Theory.

All obtained experimental data was then compared with the Von-Karman, Wagner and Generalized Wagner equations. This plot is shown in figure 3.15. For this case the Generalized Wagener theory yields a good approximation for the impact coefficient and matches closely with experimental results.

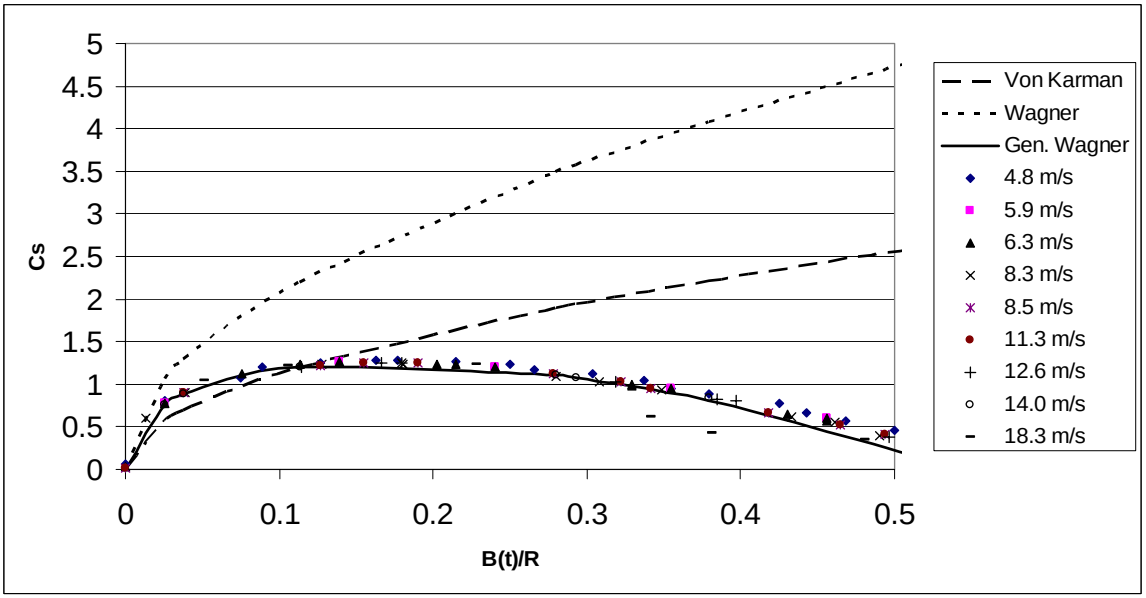

Figure 3.15 – Summary of all experimental impact coefficient data compared with the three presented theories at impact speeds ranging from 4-14 m/s. The Generalized Wagner theory is a good approximation of the experimental data.

Moghisi and Squire [14] performed similar impact tests on a 25mm diameter hemisphere fitted with a piezoelectric force transducer. They are considered to have the most elaborate and carefully obtained data available on the subject of sphere impact loads [12]. Measurements were conducted at small penetration depths of $0 < \tau < 0.25$. The Generalized Wagner theory accurately described the experimental results obtained by Moghisi and Squire.

Chapter 4

Splash Inception and Cavity Formation

4.0 – Motivation

Initially it was hypothesized that there existed a dimensionless critical speed before which no splash cavity would form, and after which the angle of the trailing water cavity would be constant for all impact velocities above that critical impact speed. Preliminary testing of the WebLab experimental setup described in chapter 2 indicated that splash cavity formation behind an impacting sphere was speed dependent. At slow impact speeds the water rode up and around the sphere creating no water cavity during the impact process. At higher velocities a cavity was formed as the sphere entered the water.

Initial test data from the drop test of a 2.54 cm (1 in) sphere is an example of this result. When dropping the sphere from a height of 0.5 meters, no splash cavity was formed. When dropping the same sphere from a height of 1.0 meters a splash cavity did form. Figure 4.1 shows two images from these trials when the sphere was roughly two ball diameters below the free surface. Dropping the sphere from 0.5 and 1.0 meters corresponds to impact velocities of 3.2 and 4.4 m/s respectively. It can be seen that no splash cavity was formed at the lower impact velocity (figure 4.1a), while there was a cavity formed at the increased impact velocity (figure 4.1b).

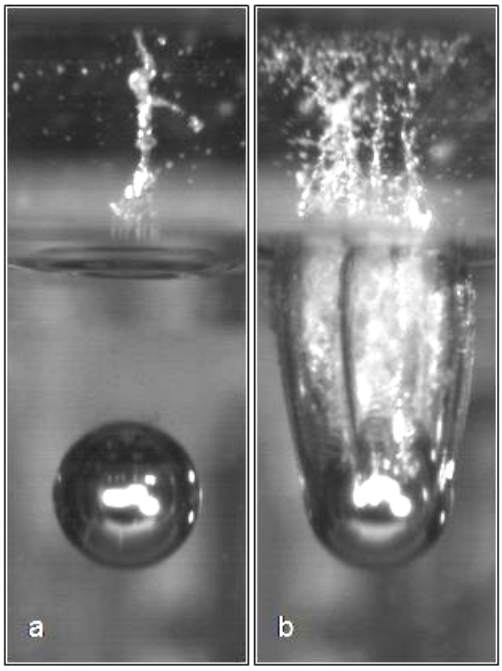

Figure 4.1 – Images of a 2.54 cm sphere impacting the free surface. When dropped from 0.5 m the sphere did not form a splash cavity (a). When the same sphere was dropped from 1.0 meters the sphere formed a fully developed cavity (b).

For the purpose of this thesis, the impacting sphere is considered to have formed a splash cavity when the cavity is clearly open to the atmospheric air at a depth of one sphere diameter below the free surface. The objective here is to determine if there existed a critical splash formation impact speed and if it was dependent on the viscous effects of the fluid, the gravitational force on the object, neither, or both. Two dimensionless parameters can be used in evaluating these effects. Reynolds number describes the ratio of inertial force to viscous force and is used in momentum, heat, and mass transfer to account for dynamic similarity. Froude number describes the ratio of inertial force to gravitational force. In general, the Froude number is used in momentum transfer, open channel flow, wave and surface behavior calculations. The Reynolds and Froude numbers are defined as:

$$\mathbb{R}_e = \frac{V_I d}{\upsilon} \qquad [4.1]$$

$$F_r = \frac{V_I}{\sqrt{gd}} \qquad [4.2]$$

Where V_I is the impact velocity of a sphere of diameter d, ν is the kinematic viscosity of the fluid, and g is the gravitational constant.

There exists little experimental data in the range of low impact velocities such as the speeds tested here. The majority of existing research has been in the high impact velocity regime which applies to the water entry of bullets and high speed missiles. Low impact velocity water surface impact brings with it an interesting and complex behavior which will be shown in the subsequent sections. The speed at which a cavity forms behind an impacting sphere as well as the angle of that formed cavity will be discussed in this chapter.

4.1 – Experimental Method

Steel spheres ranging in size from 0.64 cm (¼ in) to 5.08 cm (2 in) were used in these experiments. Each sphere was dropped at a predetermined height which would yield a desired impact velocity. For this experiment the impact velocity raged from 0 to 6.9 m/s. It was not advantageous to use the WebLab experimental setup due to the smaller scale of this experiment. Therefore, a 0.9 m x 1.2 m x 0.6 m deep aquarium was used instead of the larger water tank. A sheet of rubber lined the bottom of the tank and a piece of ultra high molecular weight (UHMW) plastic with rubber feet was placed on top. 5 cm thick foam blocks were then placed on top of the plastic. The foam was buoyant so steel weights were placed on top of the foam to sink it and prevent the foam from moving during impact. Steel weights rust quickly and had the potential of leaching rust into the water which may have changed the water properties during the course of testing. To prevent this, the weights were sealed in plastic bags. Please refer to figure 2.11 in chapter 2 for an image of this setup.

In order to drop the steel spheres from the same height, a 12 Volt cylindrical electromagnet was used. The steel spheres were held by the magnet when voltage was

applied. When the power was turned off, the steel spheres would drop. The electromagnet was attached to a rectangular bar of UHMW plastic. This assembly was then lowered or raised to give the desired drop height. Impact velocity was determined using the basic free fall physics equations:

$$D = V_i t + \tfrac{1}{2} a t^2 \qquad [4.3]$$

$$V_f = V_i + at \qquad [4.4]$$

$$V_f^2 = V_i^2 + 2ah\,, \qquad [4.5]$$

where h is the drop height of an object with initial velocity V_i, acceleration a, and drop time t. D is the distance traveled and V_f is the final velocity of the object. The final impact velocity was taken when the sphere just made contact with the water surface. In these experiments there was no initial velocity and the above equations reduce to:

$$D = \tfrac{1}{2} g t^2 \qquad [4.6]$$

$$V_f = \sqrt{2gh} \qquad [4.7]$$

The impact velocity is only a function of drop height, which was defined as the distance from the water surface to the bottom of the sphere. A steel ruler was used to measure the drop height. However, the actual impact velocity was determined by using the high speed camera images to obtain the position at each frame using the same method discussed in chapter 3. The obtained drop test position data matched the above equations to within 0.1 m/s over the range of impact velocities tested. After five such tests it was decided to use the above equations for velocity calculations instead of image processing.

Each sphere was first dropped from a zero drop height where the bottom of the sphere was positioned just above the free surface. It was found that if the ball just touched the free surface, the local water surface rode up the ball and formed a meniscus. Touching the free surface changes the surface tension which may have changed results for that data point. A zero drop height was therefore defined as the lowest height in which the ball did

not touch the free surface. The drop height was then increased by 2.54 cm (1 inch) increments up to a height of 2.4 meters. This corresponds to impact velocities ranging from 0 to 6.9 m/s. In areas where interesting phenomena occurred, such as transitional regions, the drop height increment was lowered to 0.64 cm (¼ in). During the impact force coefficient experiments in chapter 3, it was found that the lowest impact velocity tested (4.8 m/s) was more than sufficient to produce fully developed cavities for standard sized billiard balls. Therefore, the potential velocity range for this experiment was more than sufficient to obtain the transitional region of interest as well as fully developed cavities for cone angle calculations.

It was found that after power to the electromagnet was turned off, there was a lingering magnetic field. This had no effect on the larger spheres but would hold the 0.64 cm and 1.27 cm (¼ and ½ in) steel spheres to the magnet. A bar magnet was rotated close to the electromagnet which cancelled the lingering magnetic field and allowed the smaller spheres to drop with negligible effect to the impact velocity and vertical trajectory. After each test the water surface was allowed to dampen out for one minute before continuing with the next. This allowed for a consistently flat impact surface for every test.

After splash inception, pixel locations of seven points along the cavity walls were recorded as the sphere descended though the water. A linear fit was applied to these points from which the slope of the cavity wall was found. At any impact velocity the hydrostatic pressure causes the air cavity to close. However, the cavity walls can be considered linear during the first moments of impact ranging in depths from 2-10 ball diameters depending on the impact velocity. The cavity angle was taken during that time. Cone angle was defined as the total angle between the cavity walls as shown in figure 4.2.

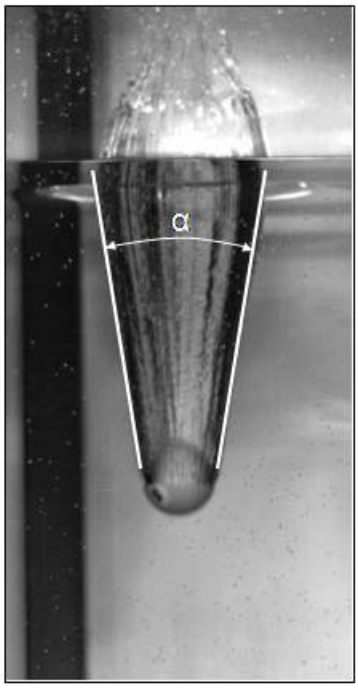

Figure 4.2 – Cone angle, α of a water cavity formed by an impacting spherical object. This image is of a pool ball at an impact speed of 5 m/s. The walls of the cavity are relatively straight during the first moments of impact which provided the reference of the cone angle

Each experiment was performed three times to test repeatability. The average angle obtained over the three tests was then calculated and used as the data point for that particular impact velocity.

4.2 – Impact Velocity Results

Impact velocities ranged from 0 m/s up to 6.9 m/s. Impact velocity was limited by the drop height, which in this case was the height of the room in which the tests were performed. Terminal velocity for a 5.08 cm (2 in) and a 0.64 cm (¼ in) steel sphere in air is approximately 91 m/s and 32 m/s respectively. The range of velocities tested in this thesis is substantially lower than terminal velocity and therefore equations 4.6 and 4.7 are accurate models of the sphere's velocity prior to impact. The first tests conducted were at a zero impact velocity. Upon entering the water, each sphere size tested created a cavity. Figure 4.3 shows the slow speed cavity formed by a 5.08 cm (2 in) sphere.

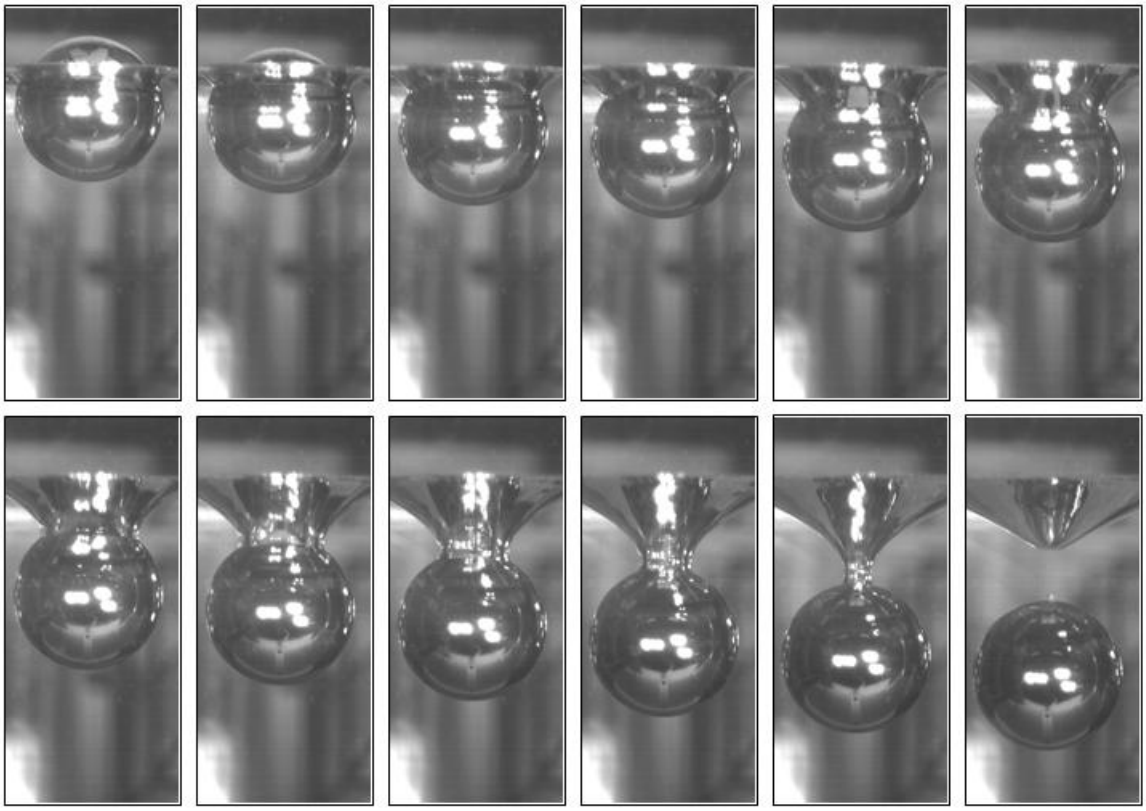

Figure 4.3 – Cavity formation from a 5.08 cm steel sphere dropped from 0 m above the free surface. These images were taken at a frame rate of 2014 Hz but every tenth frame is shown here giving an apparent frame rate of 201 Hz. Time between frames is .0497 seconds. Unlike the cavities formed at high speeds where the cavity walls are straight during the first moments of impact (see figure 4.2), slow speed cavities have curved cavity walls.

At zero impact velocity, cavity formation was effected by surface tension. The water in a sense "sticks" to the sphere and as the sphere descends through the water it drags the local water surface down with it. The cavity walls are not straight due to fact that the sphere imparts little momentum to the surrounding fluid at these low velocities. This allows the hydrostatic pressure to deform the cavity walls in the early stages of impact. The cavity then detaches when the sphere is roughly one to two diameters below the free surface.

The balls were then dropped from increasing heights. The low speed cavities did not form after the ball was dropped from about 0.3 m. At these heights, the water traveled around the sphere and closed on the top with little to no cavity formation (figure 4.4).

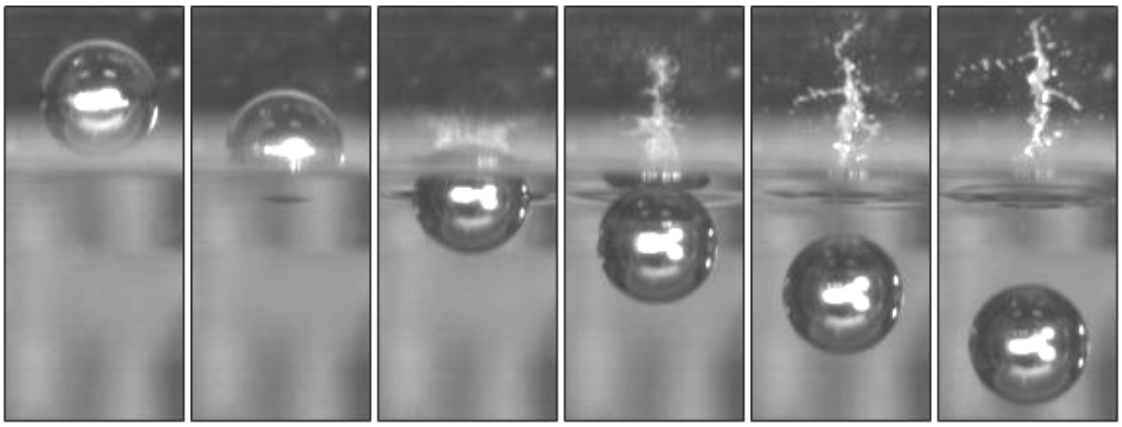

Figure 4.4 – Absence of cavity formation for a 2.54 cm diameter (1 inch) sphere at an impact velocity of 3.24 m/s. These images were taken at a frame rate of 2014 Hz but every seventh frame is shown here giving an apparent frame rate of 288 Hz. Time between frames is 0.003 seconds. At this impact velocity water rides up and around the sphere causing no cavity to form.

The spheres simply slipped through the surface of the water without forming a cavity. Critical splash formation speed was taken after the slow speed cavity was formed and the spheres slipped through the surface.

At this point it must be mentioned that there was no audible sound when the spheres slipped through the surface without forming cavities. However, when cavities were formed, slow speed cavities or otherwise, an audible noise was heard. This has obvious naval implications where the goal is to make as little noise as possible. Modifying the drop heights and impact angles of depth charges, surface torpedoes, or any air-to-water entry object could have a large effect on the acoustic noise generated upon impact.

Another interesting phenomenon was that the surface cavity did not start in the same place for each experimental run. Figure 4.5 shows five tests performed on the same 5.08 cm (2 in) sphere for the same drop height of 70 cm. For each of these runs shown, the cavity started at a random location. This phenomenon occurred over a wide range of impact speeds for each of the tested spheres without a recognizable pattern. Figure 4.5a shows no cavity, while 4.5e shows a full cavity. Figures 4.5b-c shows cavity formation

starting at different locations on the sphere. Figure 4.5d shows two separate cavities forming on different sides of the sphere.

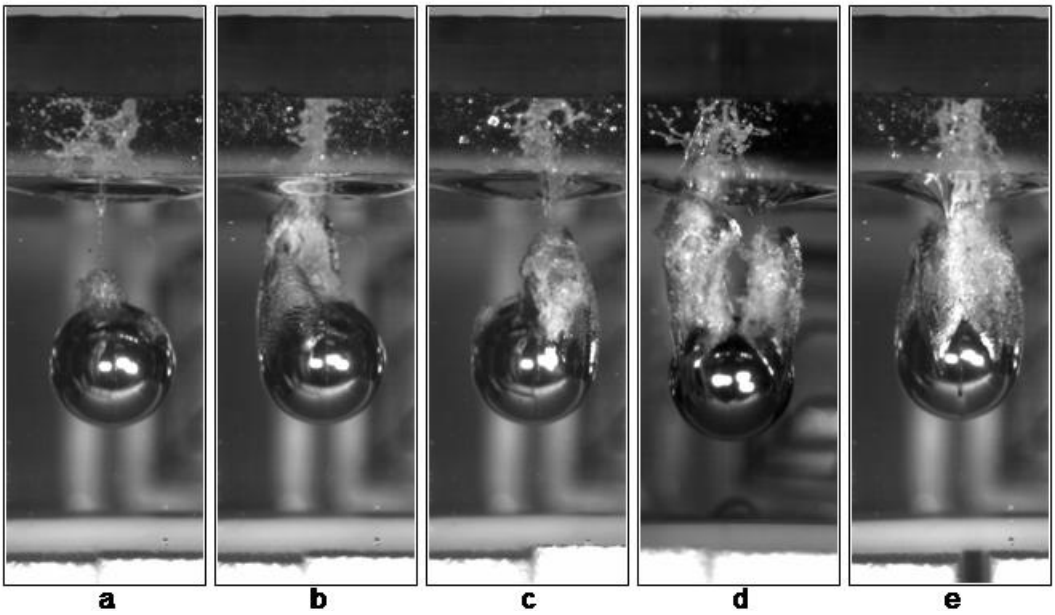

Figure 4.5 – Inconsistency of cavity initiation location for a 5.08 cm sphere at an impact speed of 3.67 m/s. This phenomenon occurred over a wide range of impact speeds for each of the tested spheres without a recognizable pattern.

At impact speeds above 5 m/s, the cavity consistently formed in-line with the balls trajectory. It is apparent that instabilities exist over a range of impact velocities for each of the sphere sizes. Possible reasons for these inconsistencies include the effects of surface tension, defects on the sphere's surface, or non-uniform water surface during impact. Gilbarg and Anderson [5] noticed the sensitive nature of the water surface condition on the formation of splash cavities. Disturbances to the symmetry of the water cavity were demonstrated where the surface was almost imperceptibly ruffled by droplets of water preceding the entry of the projectile.

Care was taken to drop the spheres only when the water surface was flat. However, no instrumentation was used to verify that the surface was completely flat before each test. A time increment of one minute was used between each test to allow the surface to dampen out. Since the water surface was not precisely controlled, it is possible that even

the smallest variation in surface condition played a larger role in splash deformation than anticipated and that even a small dust particle might have had an adverse affect on cavity formation. This may be an interesting subject of future research. In an attempt to limit these adverse affects, all drop tests were performed in one day. The water composition and surface tension were considered constant during the course of the day. Presented results may be unique to the tested water conditions; however, subsequent tests were performed on various days with different water conditions and trends were found to be generalized. Figure 4.6 below summarizes the drop test results. Triangles indicate when there was and circles indicate when there was not a surface cavity open to the atmospheric air when the sphere was one diameter below the free surface.

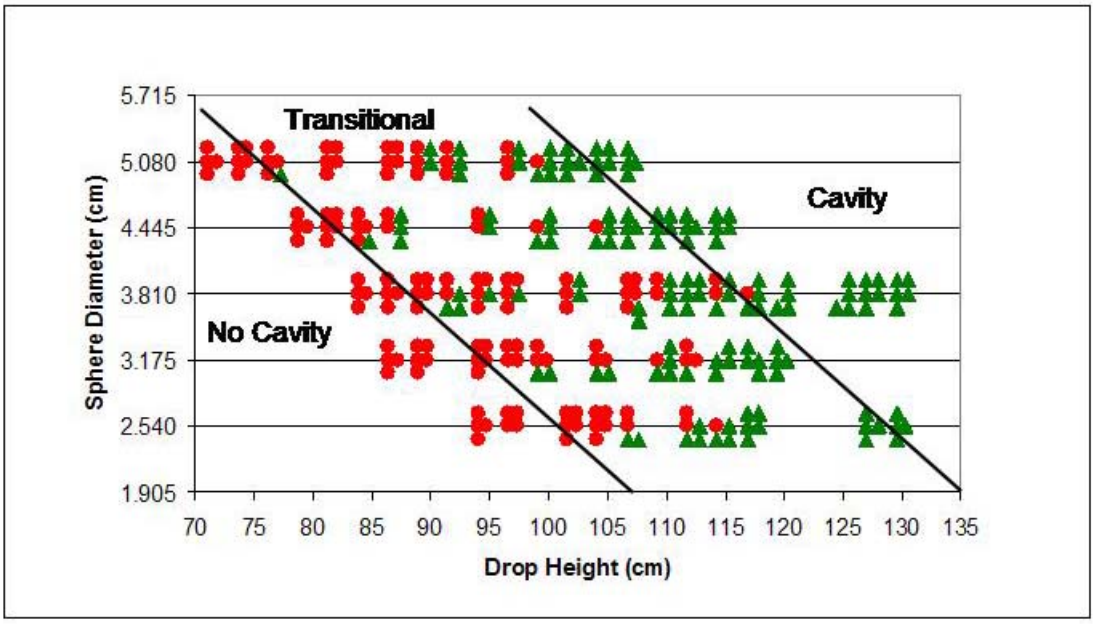

Figure 4.6 – Summary of drop test results when the sphere was one diameter below the free surface. Instabilities occurred over a wide range of impact velocities but results were consistent outside of that band.

Instabilities, such as those shown in figure 4.5, were concentrated within the transitional band shown above. Once outside of that band, results were consistent. To the left of the transitional band, no cavities were formed while on the right side of the band, cavities did form. The critical splash formation speed was evaluated on both sides of the transitional band for both Reynolds and Froude comparisons. The velocity threshold was defined as

the last speed at which the phenomena of interest were consistent. For example, the velocity on the lower bound was determined by the maximum drop height at which all trials resulted in no splash cavity formations. Figure 4.7 and 4.8 shows the Reynolds and Froude comparisons respectively.

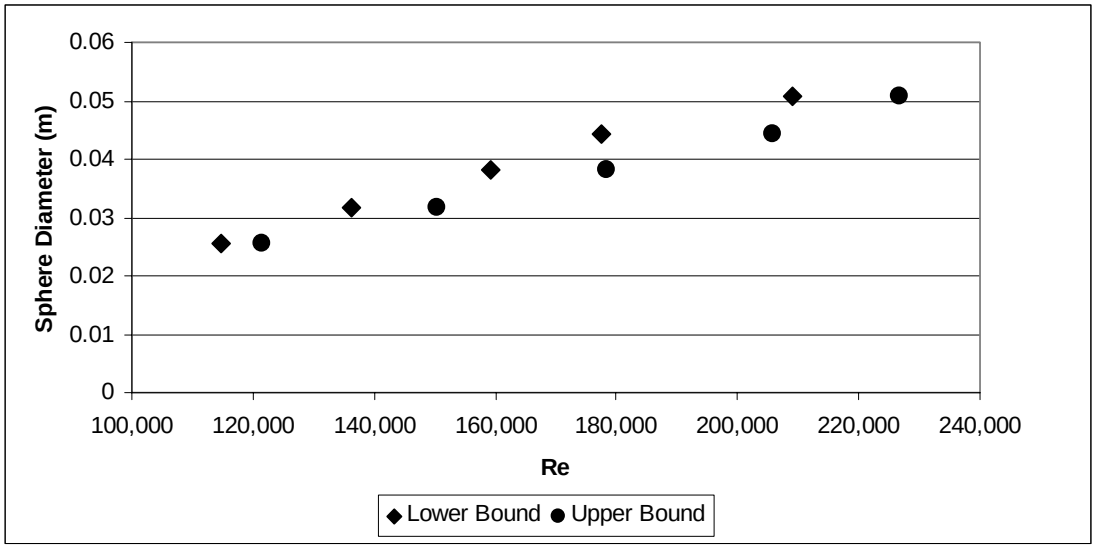

Figure 4.7 – Reynolds comparison for the upper and lower bounds of the transitional splash formation band. A linear curve fit was applied to the data points and yielded an R-Squared value very close to one.

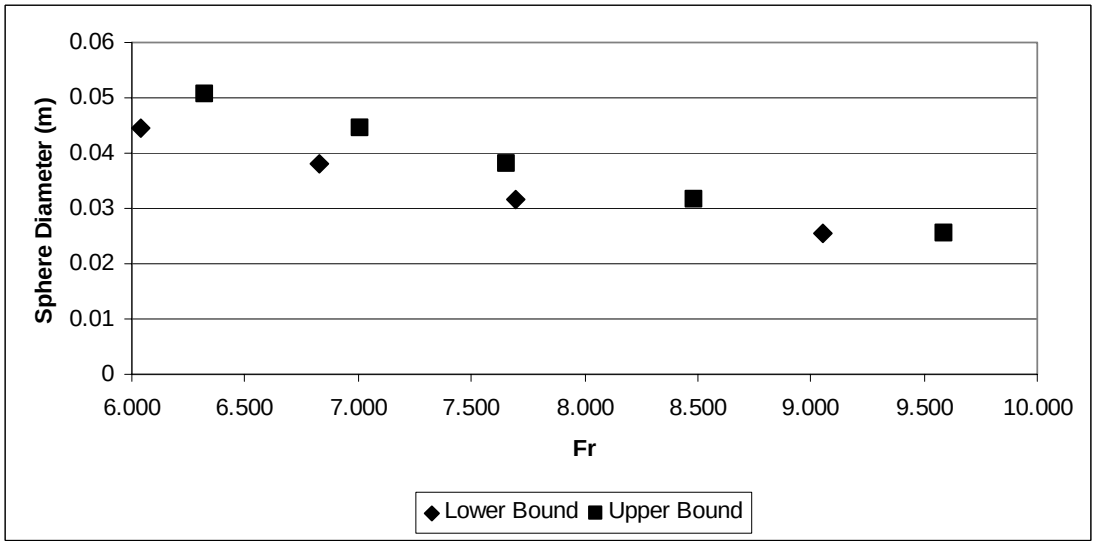

Figure 4.8 –Froude comparison of the upper and lower bounds of the transitional splash formation band. A polynomial curve fit was applied to the data points and yielded an R-squared value very close to one.

The data points in figure 4.7 can be fit with linear curves. Similarly, the data points in figure 4.8 can be fit with second order polynomials. Both sets of curve fits had R-squared values of 0.99 and higher. The R-squared value is an indicator from 0 to 1 that reveals how closely the estimated values for the curve fit correspond to the actual data. The curve fit is most reliable when its R-squared value is at or near 1. This is also known as the coefficient of determination. As can be seen, the transitional band was well defined by a linear Reynolds comparison or a polynomial Froude comparison. On either side of this band, splash cavity formation was well defined.

4.3 – Cone Angle Determination

Next, this thesis looked at the geometry of the cavity behind the sphere. All cone angle data was taken above the upper bound of the transitional splash formation band (figure 4.6) where trials produced well defined cavity geometries. Figure 4.9 shows a cavity formed in the transitional band compared with a cavity formed above the upper bound of the transitional band. Above the upper boundary, trials produced clear cavity geometries where data points were easily taken.

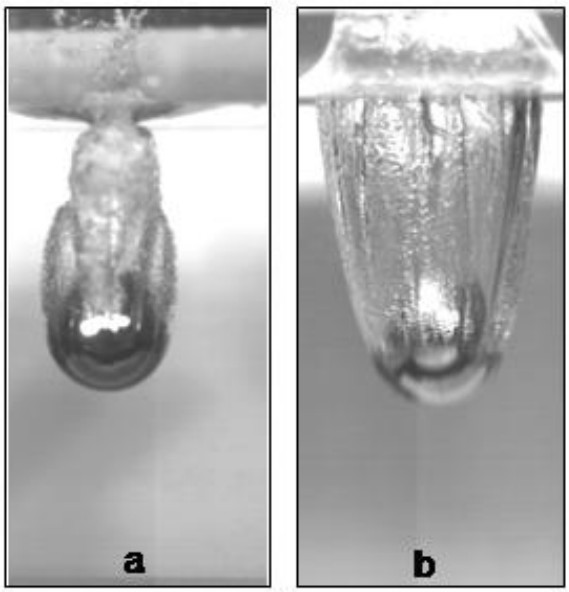

Figure 4.9 – Splash cavity formed within the transitional splash formation band for a 5.08 cm sphere at an impact speed of 4.2 m/s (a) compared with the splash cavity formed above the upper bound of the transitional band for the same size sphere at an impact speed of 6.7 m/s(b). Cavities formed outside the band produced clear and well defined geometries while cavities formed within the band did not.

As the spheres descended through the water, the cone angle changed. At the moment of impact the cone angle was the largest. The cone angle decreased as the depth increased. Figure 4.10 shows the change in cone angle of a 3.18 cm (1.25in) diameter sphere with an impact velocity of 5.2 m/s. Depth was characterized by the number of ball diameters the sphere was under the free surface. At a depth of two ball diameters (figure 4.10a) the cone angle was 23°. The cone angle decreased to 13° and 9° for four (figure 4.10b) and six (figure 4.10c) ball diameters respectively.

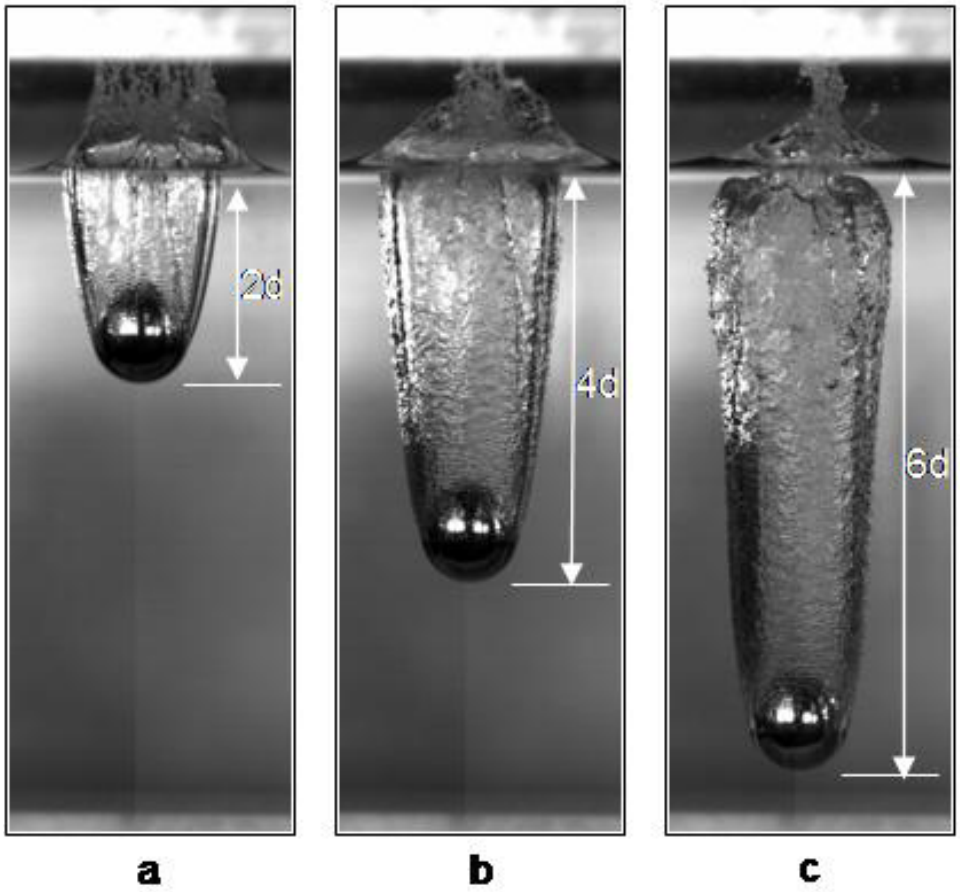

Figure 4.10 – Change in cone angle with depth for a 3.18 cm (1.25 in) steel sphere with an impact velocity of 5.2 m/s. The cone angle decreases as the sphere descends through the water from 23^{o} at 2 ball diameters depth to 13^{o} at 4 ball diameters depth and 9^{o} at 6 ball diameters depth.

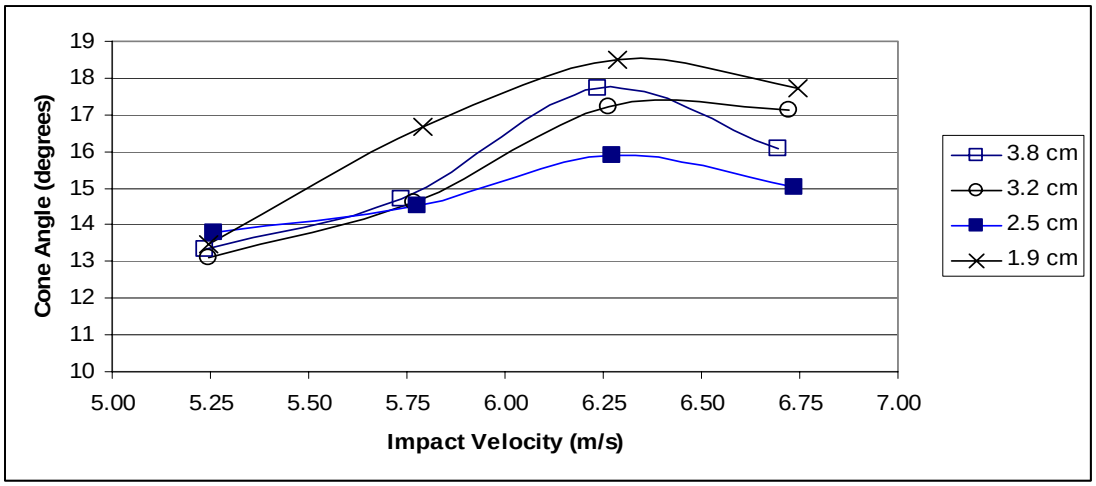

Figure 4.11 – Cone angle data for a variety of spheres over a range of impact velocities at a depth of four ball diameters. The general trend indicated an initial increase in angle with an increase of impact velocity but then decreased after a local maximum. The cone angle remained within a 5 degree window but the cone angle cannot be considered constant.

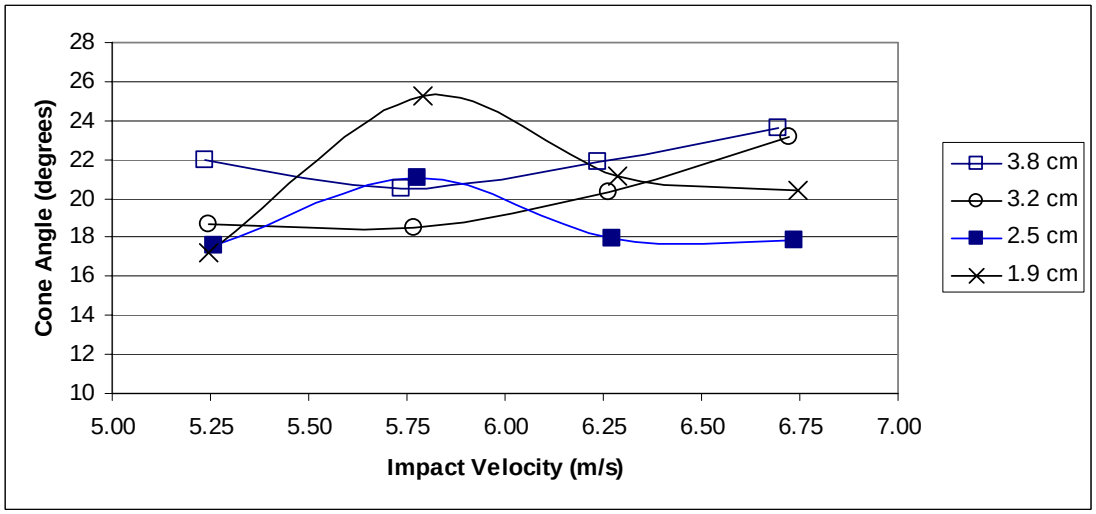

Figure 4.12 – Cone angle data for a variety of spheres over a range of impact velocities at a depth of two ball diameters. At this depth there exists no general trend and data appears scattered.

Figures 4.11 and 4.12 show the cone angle for ball depths of four and two diameters respectively. Over the relatively small range of impact speeds tested, the cone angle increased with an increase in impact velocity. This is most likely due to the increased horizontal component of impact force generated from the curvature of the ball as it descends through the fluid. However, the general trend from figure 4.11 indicated that at

a depth of four ball diameters, the angle decreases again after an impact velocity of roughly 6.3 m/s. This may be explained by the decrease in momentum transfer as the ball decelerates. Thus, there may exist a local maximum cone angle based on impact speed. Figure 4.12 shows this same behavior for the 2.5 and 1.9 cm spheres for the first two data points but for the most part the data taken at this depth appears scattered. It is clear that there exists a change in cone angle with respect to depth. To further evaluate this, cone angle data was then taken for each sphere as it descended through the water for a constant drop height. Figure 4.13 shows the change in cone angle for various spheres, which were dropped from 2.3 m, corresponding to an impact velocity of 6.7 m/s for each sphere.

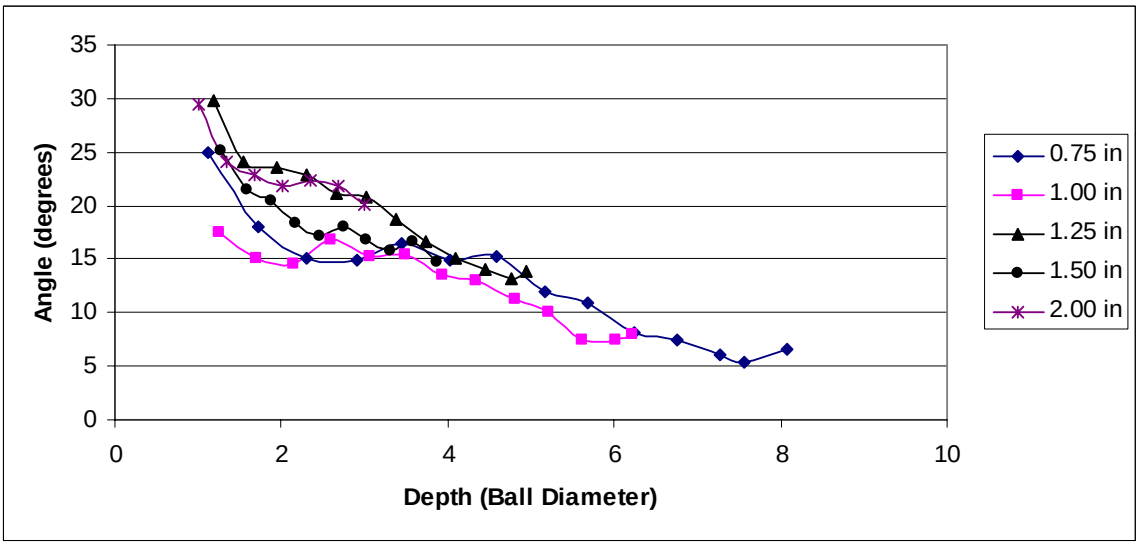

Figure 4.13 – Cone angle data for a drop height of 2.3 m (91 in). All tested spheres exhibited the same decreasing trend. After a depth of roughly three ball diameters, data appears to follow the same path.

Figure 4.13 shows a decreasing cone angle trend as each of the spheres descended through the water. The largest cone angle is seen at the beginning of impact. At a depth of two ball diameters, cone angle data was scattered over a 10 degree window which complements the observations made from figure 4.12. At this depth the cavity was still forming and exhibited volatile behavior, which explains some of the scatter. As the ball descends, the water cavities converge to follow the same general trend.

It was also noticed that between the depths of two and four ball diameters, the cone angle levels off at a nearly constant value. This is specifically apparent in the 1.91 cm (0.75 in) sphere (data represented by diamonds in figure 4.13). Such behavior may be due to a change in radial momentum transfer to the surrounding water. When the ball first impacts the free surface the water is pushed downwards and then radially outward, due to the curvature of the ball, as the ball descends through the water. At this impact velocity, the imparted momentum is sufficient to form an air cavity behind the sphere. As the sphere continues to descend, momentum transfer decreases due to sphere deceleration, thus causing a decrease in cone angle. The ball eventually reaches a terminal velocity by which time the cavity starts to close off at the surface and the cavity walls start to lose their linear characteristics.

Figure 4.14 shows position and velocity data verses time of an impacting 5.72 cm sphere from the moment it was dropped from 60 cm until it reached a depth of about 12 ball diameters. Depth was again characterized by the number of ball diameters the sphere was in relation to the free surface, which is denoted by the $z = 0$ line. Positive z represents air above the interface and negative z represents water. Air position data in figure 4.14a agreed with the general free fall equations shown in equation 4.7. Position data was obtained using the same graphical method from chapter 3. The results were then differentiated with respect to time to yield the velocity curves plotted in figure 4.14b.

At depths of roughly two and six ball diameters, there was a noticeable change in the velocity profile (figure 4.14b). The change at two ball diameters indicated a transition from impact velocity to a fairly linear decrease in velocity. This negative linear trend, which also represents a constant deceleration, continued until about five ball diameters. At this point, velocity changed to an almost constant value which indicates a transition to a terminal velocity. Using basic force balance equations, the terminal velocity of this sphere, without the influence of an attached air bubble, was calculated to be 110 cm/s.

The inflection points on the velocity curve (figure 4.14b) also correlate with the cone angle data (figure 4.13). The nearly constant value of cone angle which exists between the depths of two and four ball diameters corresponds to the linear decrease in velocity in that region. After six to eight ball diameters the sphere started to transition to terminal velocity and in most cases the cavity has closed near this point, therefore, further data was neglected. There appears to exist a close relationship between the change in velocity of the sphere and the angle of the trailing water cavity.

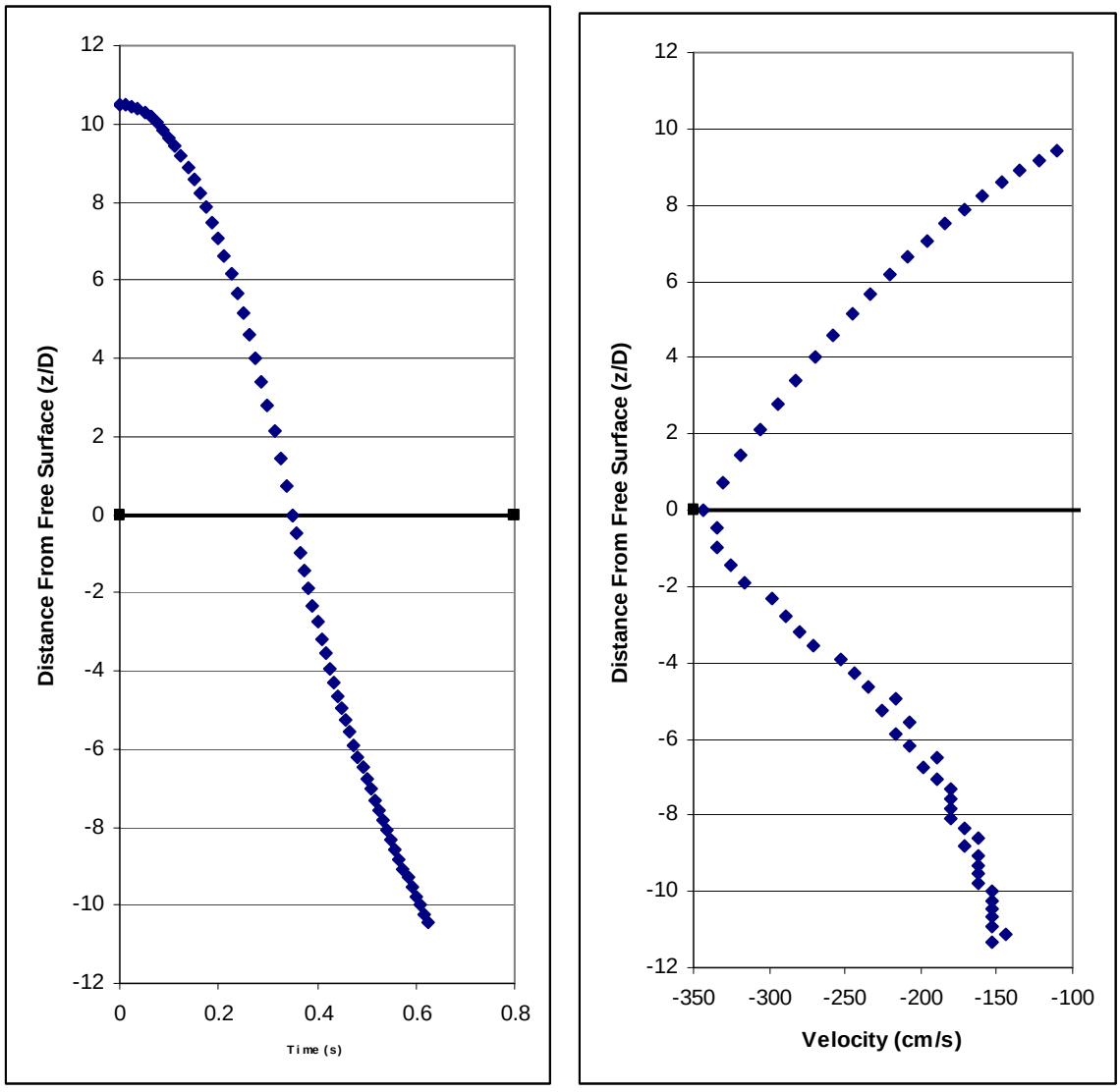

a. b.

Figure 4.14 – Position and velocity data throughout the impacting process for a 5.72 cm sphere being dropped from 60 cm. The free surface is denoted by the z = 0 line. General trends in this data shed insight into the change in cavity angle as the sphere descends through the water.

Possible sources of error in the cone angle calculations included protrusions that existed on the cavity walls in some of the trials. These protrusions tended to increase or decrease the wall angle by as much as 1-2 degrees, thus skewing the overall results. The protrusions may have been caused by instabilities in the fluid flow around the sphere or by small surface deformations on the sphere itself. The protrusions were more prevalent in the early stages of cavity formation. Cavities at a two ball diameter depth were not yet fully developed and contained many and more pronounced asymmetries. An example of these local protrusions is shown in figure 4.15.

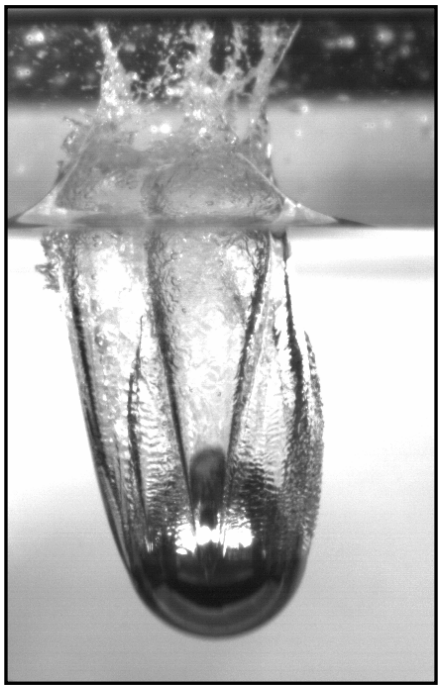

Figure 4.15 – Example of striations and protrusions found in some of the performed experiments. These local protrusions may have been caused by instabilities in the cavity wall or by small surface deformations on the projectile. This particular trial was not used as a data point and was repeated.

At depths of two and four ball diameters, it was not uncommon for the cavity to be asymmetric, which may also have skewed results. In one trial at a depth of four ball diameters, the difference in angle from one side of the cavity wall to the other was as much as 2 degrees. At a depth of two ball diameters, this difference was as much as 7 degrees. Figure 4.16 compares an asymmetric case with a symmetric case. Figure 4.16a

shows a difference in cone angle of 7 degrees between the two walls, while there is no difference in cone angle in figure 4.16b. In severe trials such as the one shown below (figure 4.16b), the run was thrown out and repeated.

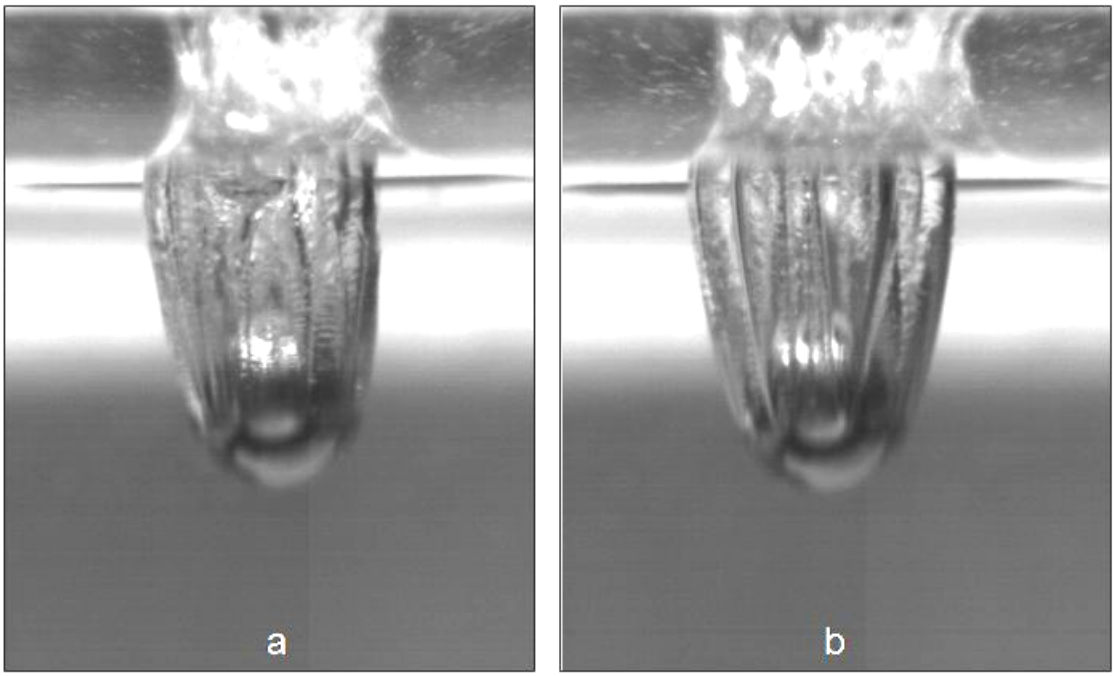

Figure 4.16 – Asymmetry in cone angle from a drop test of a 2.54 cm (1.0 in) sphere with an impact velocity of 6.3 m/s at a depth of two ball diameters. In one trial the difference in cone angle from opposing walls was as much as 7 degrees (a). Near symmetric cases were used for data (b).

From the previous two figures it is noticed that the cavity wall was not uniform and contained noticeable instabilities which start where the fluid separates from the sphere and have been noticed even on the splash sheet above the free surface. In events such as these, the particular trial was repeated and not used as a data point. However, the presence of this behavior indicates that there are instabilities present which may cause deviations in any test. Even with the occasional protrusion and asymmetry in the cone wall, trends were consistent. It was concluded that the cone angle was not constant over the range of impact velocities and depths tested. However, trends shown in figures 4.11 – 4.14 show a direct correlation between cone angle and sphere velocity. These trends were also found to be comparable for each sphere as a function of dimensionless depth.

Chapter 5

Conclusions

5.0 – Summary of Results

This thesis looks at the impact of spherical objects on the free surface with applications to ship slamming and weapon delivery. A unique laboratory facility was used for these experiments. The iMarine WebLab apparatus was designed and built in conjunction with this thesis, including an automated loading system, RPM sensors for the shooter wheels and break beam sensors to determine the initial velocity of the object upon leaving the shooter.

Experiments were performed and obtained data was compared with theoretical predictions developed by Von-Kármán and Wagner. It was clear that, up to one-half ball diameter submergence, the experimental data closely matched the predictions given by a generalized Wagner theory. Force measurements based on sphere deceleration were impossible due to the fact that the velocity during the event time of interest was constant for the type of sphere used in this experiment. Therefore, high speed imaging was used to obtain the experimental data.

Impact tests were also performed on various sized spheres over a range of impact velocities up to 6.9 m/s in order to determine a critical splash formation speed parameter. Instabilities were seen over a range of impact velocities for each of the spheres tested. At impact speeds above and below this instability band, splash formation was found to be constant and predictable. This transitional band scaled linearly with Reynolds number.

Above the critical splash formation velocity, experiments were performed to evaluate the cone angle of the cavity behind the projectile. Over the range of speeds tested the cone angle was not constant, but decreased with depth due to the external forces acting on the cavity. Between impact and two sphere diameters under the surface, the cavity angle decreased sharply. Between two and four ball diameters depth, the cone angle was approximately constant. The cone angle then decreased again until six diameters where the cavity started to close. The cone angle was not considered after cavity seal occurred and the bubble pinched off. At this point the entrained air cavity did not have defined cone characteristics.

Most noteworthy was the correlation between cone angle geometry and projectile velocity. Data in chapter four showed that the region where the cone angle plateaus corresponds to a region of linearly decreasing velocity. Above two diameters depth, the velocity decreased non-linearly as energy was transferred to the water and the upward splash and vapor cavities began to form. Once formed, the cone angle increased at a steady rate. As the ball decelerated linearly, the cone angle remained constant. After this point the cone angle resumed its decreasing trend until it finally separated from the free surface. The cone angle was clearly dependent on the change in velocity of the ball.

5.1 – Interesting Phenomena

Many additional interesting phenomena were encountered during experimentation that merit mention. For example, images of the air cavity behind a projectile as it entered the water revealed unsteady events which emerged both within the cavity and at the air-water interface as the cavity formed. Figure 5.1 shows an image of the cavity behind a 4.45 cm (1.75 in) sphere being dropped from a height of 1.14 m (45 in). Of interest are the

patterns on the air-water interface, the resulting splash features, the effect of the splash falling back to the surface, the formed surface wave, and the striations, or legs, that originate where the fluid detaches from the sphere.

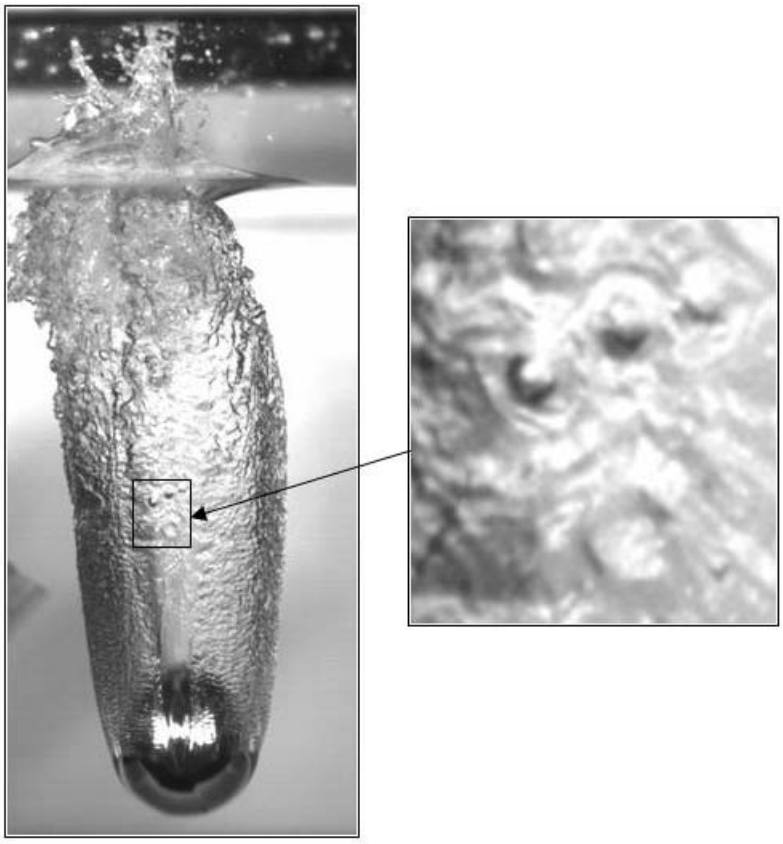

Figure 5.1 – Cavity formed by a 4.45 cm (1.75 in) sphere impacting the free surface at 4.7 m/s. Cavities formed by impacting spheres contain many interesting and violent phenomena.

In addition to simple drop tests, the Weblab apparatus was capable of applying spin to the projectiles. A rotational velocity was placed on a billiard ball by holding one wheel stationary while spinning the other. The ball would impact the free surface with a vertical trajectory but immediately start to curve. High speed imaging was used to capture the evolution of the ball's trajectory and the trailing vapor cavity (figure 5.2).

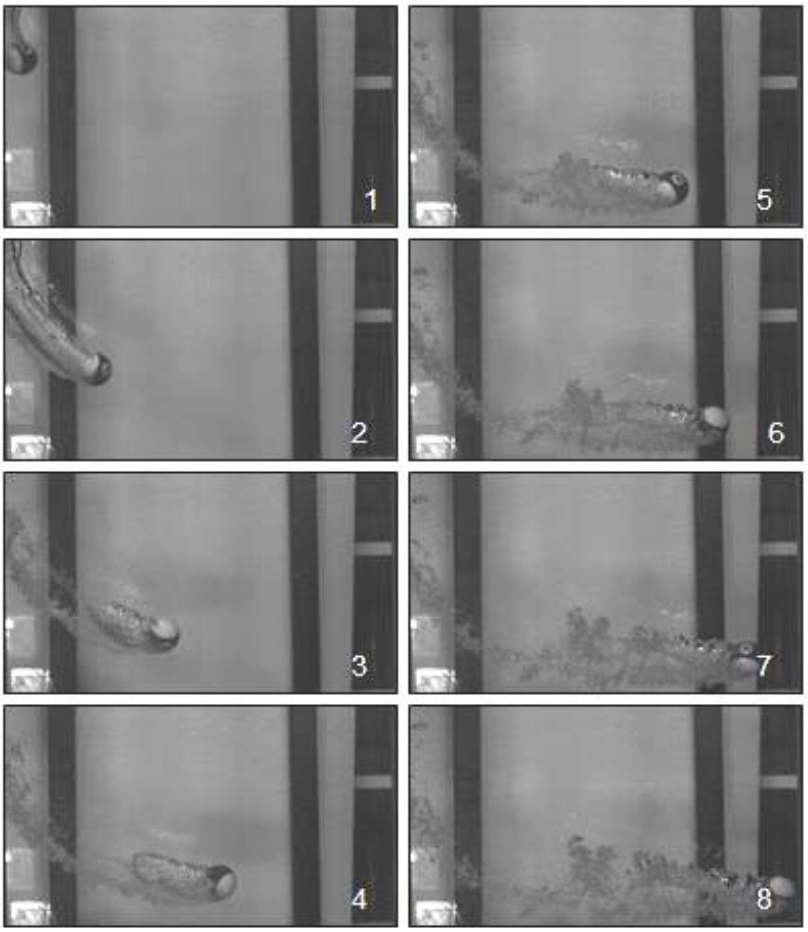

Figure 5.2 – Sequence of images showing the curved trajectory of a billiard ball with an initial rotational velocity. The billiard ball was given spin by holding one of the shooting wheels stationary while spinning the other at 1700 RPM. The camera frame rate was 629 frames per second. Every 23rd frame is included here, which gives an effective rate of 27 frames per second.

Curve balls in air take a relatively long distance to become noticeable. Since water is 1000 times denser than air, these events occur in a much shorter distance, making the event easier to capture on camera. The lift, L, of a 2-dimensional body is given by:

$$L = \rho v \Gamma \qquad [5.1]$$

where ρ is the fluid density, v is the velocity of the object with a rotational velocity, Γ. A general solution to the lift generated by a rotating sphere is not this straightforward due

to the complex three-dimensionality of the problem. This problem would make for an interesting underwater baseball game.

During the initial design of the WebLab experimental setup, the possibility of the projectiles skipping off the free surface if given too much freedom in impact angle was evaluated. For this and other reasons the impact angle was limited to 15 degrees from vertical. The surface skipping characteristics of various shaped geometries is another interesting area of research [10]. Characteristics of rock skipping have been recorded since the times of the ancient Greeks [3] and as recently as 2003[2]. Experimental observations have been used to augment warfare tactics from the 16^{th} to the 19^{th} centuries. In some seafaring situations gunners would aim for the water surface such that the ricochet would hit the target producing an angle of incidence which seemed to cause more damage than a direct hit [7].

It is easy to see why the problem of impact on a free surface has piqued the interest of researchers for centuries. The complex yet beautiful hydrodynamic phenomena taking place during impact contain many applications from recreational sports to the design of full sized ocean vehicles. Countless hydrodynamic problems remain unsolved and until they are, hydrodynamics will continue to capture the attention of scientists from around the world.

Bibliography

[1] K. Asfar and S. Moore. Rigid-Body Water Impact at Shallow Angles of Incidence. *Proceedings of the International Offshore Mechanics and Arctic Engineering Symposium*, Vol. 2 pp. 105-112, 1987

[2] L. Bocquet. The Physics of Stone Skipping. *American Journal of Physics*, Vol. 71, No. 2, February, 2003

[3] C. Clatnet, F. Hersen, and L Bocquet. Secrets of Successful Stone-Skipping. *Nature*, Vol. 427, Pg. 29, January 1, 2004

[4] R. Cointem. Two-Dimensional Water-Solid Impact. *Journal of Offshore Mechanics and Arctic Engineering.* Vol. 111, Issue #2, May 1989.

[5] D. Gilbarg and R. Anderson. Influence of Atmospheric Pressure on the Phenomena Accompanying the Entry of Spheres into Water. *Journal of Applied Physics*. Volume 19, Number 2, pp 127-139, February 1948.

[6] J. W. Glasheen and T.A. McMahon. Vertical Water Entry of Disks at Low Froude Numbers. *Phys. Fluids*. Vol. 8, Number 8, pp 2078-2083, August 1996.

[7] S. Johnson. Ricochet of Non-Spinning Projectiles, Mainly From Water; Part I: Some Historical Contributions. *International Journal of Impact Engineering*. Vol. 21, Nos. 1-2, pp. 15-24, 1998

[8] D. Karagiozova. Dynamic Buckling Of Columns Due To Slamming Loads. *Proceedings of the 1996 4th International Conference on Structures Under Shock and Impact.* SUSI 96, July 1996, Udine, Italy

[9] A. May. Vertical Entry of Missiles into Water. *Journal of Applied Physics.* Vol. 23, Number 12, pp 1362-1372, December 1952.

[10] X. Mei, Y. Liu, and D. Yue. On the Water Impact of General Two-Dimensional Sections. *Applied Ocean Research.* Vol. 21 pp. 1-15, 1999.

[11] T. Miloh and Y. Shukron. Ricochet Off Water of Spherical Projectiles. *Journal of Ship Research.* Vol. 35, Issue #2, pp. 91-100, June 1991

[12] T. Miloh. On the Initial-Stage Slamming Of A Rigid Sphere In A Vertical Water Entry. *Applied Ocean Research*. Vol. 13, pp. 43-9248, 1991

[13] T. Miloh. On the oblique Water-Entry Problem of A Rigid Sphere. *Journal of Engineering Mathematics*. Vol. 25, pp. 77-92, 1991

[14] M. Moghisi and P.T. Squire. An Experimental Investigation Of The Initial Force Of Impact On A Sphere Striking A Liquid Surface. *Journal of Fluid Mechanics*. Vol. 198, pp. 133-146, 1981

[15] J.N. Newman. Marine Hydrodynamics, pages 358-373, 1977

[16] M.K. Ochi and L.E. Motter. Prediction of Extreme Values of Impact Pressure Associated With Ship Slamming. *Journal of Ship Res.* Vol. 13, No. 2, 1969

[17] Seeing the Unseen: Dr. Harold E. Edgerton and the Wonders of Strobe Alley. Rochester, NY, Pub Trust of George Eastman House; Cambridge, MA, Distributed by MIT Press, c1994

[18] A.W. Troesch and C.G. Kang. Hydrodynamic Impact Loads on Three-Dimensional Bodies. *Sixteenth Symposium on Naval Hydrodynamics,* pages 537-558.

[19] T. Von Karman. The Impact on Seaplane Floats During Landing. NACA TN 321, October 1929.

[20] H. Wagner. Uber Stoss – und Gleitvorgange an der oberflacke von flussigkiten. ZAMM, band 4, heft 4, 1932, pages 193-235.

[21] S. Watanabe. Resistance of Impact on Water Surface. *Institute of Physical and Chemical Research—Scientific Papers*, Vol. 23, Issue #23, pp. 202-282, February 1934.

[22] I. Wantanabe. Theoretical Investigation on the Wave Impact Loads on Ships. *Proceedings from the Sixteenth Symposium on Naval Hydrodynamics*. Pp. 559-574.

[23] A.M. Worthington. A Study of Splashes. Longmans Green and Company, New York, 1908.